Coseismic slip model of offshore moderate interplate earthquakes on March 9, 2011 in Tohoku using tsunami waveforms

Tatsuya Kubota[a*], Ryota Hino[a], Daisuke Inazu[b1], Yoshihiro Ito[c], Takeshi Iinuma[d], Yusaku Ohta[a], Syuichi Suzuki[a], Kensuke Suzuki[d]

[a] Graduate School of Science, Tohoku University, 6-6, Aza-Aoba, Aramaki, Aoba-ku, Sendai 980-8578, Japan.

[b]U Tokyo Ocean Alliance, The University of Tokyo, Tokyo, Japan.

[c]Disaster Prevention Research Institute, Kyoto University, Uji, Japan.

[d]Japan Agency for Marine-Earth Science and Technology, Yokohama, Japan.

[1]Present address: Department of Ocean Sciences, Tokyo University of Marine Science and Technology, Tokyo, Japan.

E-mail addresses:

Tatsuya Kubota: tatsuya.kubota.r6@dc.tohoku.ac.jp

Ryota Hino: hino@m.tohoku.ac.jp

Daisuke Inazu: inazud@oa.u-tokyo.ac.jp

(Present e-mail address: inazud@m.kaiyodai.ac.jp)

Yoshihiro Ito: ito.yoshihiro.4w@kyoto-u.ac.jp

Takeshi Iinuma: iinuma@jamstec.go.jp

Yusaku Ohta: yusaku.ohta.d2@tohoku.ac.jp

Syuichi Suzuki: syuichi.suzuki.a1@tohoku.ac.jp

Kensuke Suzuki: kensukes@jamstec.go.jp

[*]Corresponding author E-mail: tatsuya.kubota.r6@dc.tohoku.ac.jp

Abstract

We estimated the coseismic slip distribution associated with the Mw 7.2 and 6.5 foreshocks of the 2011 Tohoku-Oki earthquake based on analysis of the tsunami waveform records obtained just above their focal areas. The results show that the main rupture areas of each of the foreshocks do not overlap with each other, and show a distribution that is complementary to the postseismic slip area of the first Mw 7.2 foreshock as well as to the epicenters of smaller earthquakes during foreshock activity. After the second largest foreshock, seismicity increased in the area between the rupture area of the second largest foreshock and the mainshock epicenter, suggesting propagation of aseismic slip towards the mainshock epicenter. The calculated stress drop of the second largest foreshock was smaller than the largest one, implying strength reduction during the postseismic period of the largest foreshock. Based on a comparison of coastal tsunami records, it is suggested that the asperity ruptured in the M 7.0 earthquake in 1981 ruptured again during the largest foreshock in 2011, but it expanded to the updip side of the 1981 rupture area and became larger in magnitude, exemplifying the irregularity of earthquake recurrence in the area.

Keywords: 2011 Tohoku-Oki earthquake, foreshock, tsunami, subduction zone, seafloor observations

Highlights

- Finite fault models of two large 2011 Tohoku earthquake foreshocks are presented

- Nearest-field tsunami data inversion revealed coseismic slip of the foreshocks
- South-migrating seismicity suggests aseismic slip triggered the Tohoku earthquake
- Foreshock coseismic and postseismic slip areas show complementary distributions
- A 1981 M7 earthquake asperity ruptured during the largest foreshock in 2011

1. Introduction

The 2011 Tohoku-Oki earthquake occurred at 5:46 UTC on March 11, 2011 (hereafter, the mainshock). The mainshock was preceded by intensive foreshock activity, including the largest foreshock (Mw 7.3, Global CMT, http://www.globalcmt.org) and the second largest foreshock (Mw 6.5, Global CMT) that occurred at 2:45 and 21:24, respectively, on March 9, 2011. Hereafter, we refer to the largest foreshock as foreshock #1 and the second largest foreshock as foreshock #2. The location of the epicenters and focal mechanisms of the mainshock and the two major foreshocks are shown in Figure 1. The epicenters of foreshock #1 and foreshock #2 were located ~50 km northeast and ~20 km northeast of the mainshock epicenter, respectively. The focal mechanism solutions of the two foreshocks closely resemble each other, indicating that the two events can be regarded as failures of a plate boundary fault with the same slip direction.

Although a number of finite source models of the mainshock have been presented (e.g., Ide et al., 2011; Ozawa et al., 2011; Saito et al., 2011; Simons et al., 2011; Iinuma et al., 2012; Satake et al., 2013), few studies have attempted to show the source model of foreshock #1. Shao et al. (2011) estimated the coseismic slip distribution of foreshock #1 based on joint inversion of seismic and GNSS data, and Gusman et al. (2013) analyzed offshore tsunami waveform records associated with foreshock #1 to obtain its finite fault model. Ohta et al. (2012) modeled the geodetic records of onshore GNSS stations and ocean bottom pressure gauges (OBPG) to derive the coseismic fault model of foreshock #1, as well as its postseismic slip distribution. The estimated postseismic slip occurred on the plate boundary where a sudden increase in seismicity was observed, regarded as the aftershocks of foreshock #1. Ando and Imanishi (2011) found that the seismicity expanded from the source area of foreshock #1 and the mainshock rupture was initiated when it reached the mainshock hypocenter. Kato et al. (2012) pointed out that the southward migration of the aseismic slip occurred just after foreshock #1 and initiated rupture of the mainshock. All these studies suggested that there was a chain-reaction interplay between the aseismic slip and the small earthquakes emerging after foreshock #1 in the surrounding region, and that the activity facilitated rupture initiation of the Mw 9 mainshock.

Foreshock #2, which occurred between the epicenters of foreshock #1 and the mainshock (Figure 1), can be regarded as the largest aftershock of foreshock #1 and could have been triggered by its aseismic afterslip. Therefore, the rupture process of foreshock #2 will provide additional information for characterizing the dynamic processes preceding the 2011 Tohoku-Oki earthquake around its epicenter. However, little is known about foreshock #2 because of its size, which is too small for finite source modeling using available onshore seismic, geodetic, and coastal tsunami data. When the two foreshocks occurred, nine ocean bottom pressure gauges (OBPGs) were deployed just above the focal area (Figure 1, Table 1) and they recorded clear pressure changes associated with sea surface motions due to tsunamis as well as coseismic static displacement of the seafloor (Figure S1) during the two foreshocks. In this study, we analyze the OBPG data to obtain finite source models for the two major foreshocks.

Tsunami data are often used to estimate the initial tsunami height distribution and source models of tsunami-generating earthquakes (e.g., Saito et al., 2011; Tsushima et al., 2012; Satake et al., 2013; Inazu and Saito, 2014; Kubota et al., 2015). Among a number of approaches for obtaining earthquake source models, tsunami waveform inversions have an advantage over inversions using seismic data because the spatial distribution of tsunami propagation speed is much better known than that of seismic waves. Accurate models of tsunami wave propagation allow us to make more reliable waveform calculations and to increase the robustness of obtained source models. When tsunami waveforms are obtained far offshore, the inversion results will be more reliable compared to those using coastal tsunami data because offshore waveforms are almost free from the nonlinear and complex behaviors due to coastal interaction. Several previous studies have demonstrated that finite source models of moderate earthquakes (Mw ~ 7 or smaller) could be derived from offshore tsunami data (e.g., Hino et al., 2001; Tanioka et al., 2007; Saito et al., 2010). We use offshore near field tsunami records obtained by OBPG that are more reliable than coastal records to inspect the source processes of the two foreshocks.

The purpose of this study is to obtain fault models of foreshocks #1 and #2 of the 2011 Tohoku-Oki earthquake using OBPG records, and to discuss the spatio-temporal evolution of foreshock activity driven by aseismic slip thought to trigger the Mw 9 mainshock.

2. Ocean Bottom Pressure Data

Seven offshore OBPGs were deployed around the foreshock activity zone by Tohoku University and were in operation in March 2011 (Figure 1 and Table 1). Those OBPGs were offline autonomous instruments with pop-up recovery. We deployed the instruments at stations GJT3, P02, P03, P06, P07, P08, and P09, located within ~70 km of the epicenters of the foreshocks. Detailed descriptions of the instruments are given in Hino et al. (2014). Although the tsunamis associated with the foreshocks were also observed at TM1 and TM2, pressure-recording nodes of real-time cabled observation systems operated by the Earthquake Research Institute of the University of Tokyo (Kanazawa and Hasegawa, 1997) (Figure 1 and Table 1), we did not use them to estimate the fault models of the foreshocks. This is because they were located more than 100 km away from the epicenters.

Figures 2 and 3 show the pressure records obtained after the following data processing. First, pressure changes caused by ocean-tides were removed from the observed time series. Ocean-tide variations were computed using a theoretical tide model, NAO.99Jb, developed by Matsumoto et al. (2000), assuming that a 1 cm water height anomaly was equivalent to 1 hPa of pressure change. After the de-tiding process, we took the moving average with a 60 s time window, then applied a low-pass filter (Saito, 1978) with a cutoff frequency of 2.5 mHz (=1/400 Hz) in order to remove high frequency components associated with elastic waves both in the seawater and beneath the seafloor generated by earthquakes. Examples of the observed and processed waveforms are shown in Figure S1.

The observed tsunami waveforms associated with foreshock #1 are very clear and simple, composed of a pair of up-motion and subsequent down-motion waveforms (Figure 2). The width of the up-motion pulse is ~8 min. The highest water level exceeds 20 cm (corresponding to a 20 hPa pressure increase) at station P06. On pressure records of several stations, clear permanent steps associated with vertical seafloor displacement can be identified. The records at P02 and P06 show pressure increases of ~10 hPa, indicating ~10 cm of subsidence, whereas a pressure decrease of ~10 hPa, corresponding to uplift of ~10 cm, was observed at P09.

The tsunami from foreshock #2 (Figure 3) has a much smaller amplitude than that of foreshock #1. The tallest height was ~3 cm, observed at P02 and P03. The waveforms also appear simple, although the low signal-to-noise ratio makes it difficult to inspect the waveform characteristics in detail. The duration of the up-motion pulse was ~5 min. Evident coseismic uplift, as large as 4 cm, was recorded at P09 as a pressure reduction of ~4 hPa, larger than the previously reported noise level (Inazu and Hino, 2011) of the seafloor pressure records obtained by pressure sensors with the same performance as those of the OBPGs used in the present study. However, the smaller (<1 hPa) offset changes in other records could be apparent because of long-period noise.

The durations of the up-motion part of the observed tsunami waveforms enable us to guess approximate source sizes based on the propagation speed at the source region. Based on linear long-wave theory, the tsunami wave speed v is expressed as $v = \sqrt{gH}$, where g is the gravity acceleration constant (=9.8 m/s^2) and H is the water depth (e.g., Satake, 2002). Water depth in the source region is ~2,000 m so the tsunami wave speed can be approximated as ~140 m/s. From the observed pulse widths, the spatial dimensions of the uplift area can be roughly estimated as ~60 km for foreshock #1 and ~40 km for foreshock #2.

3. Methods

In order to obtain the coseismic slip distribution, we carried out a tsunami waveform inversion using the OBPG records. We used the 1-Hz sampled pressure time series with a time window of 20 min from the origin time, as determined by Suzuki et al. (2012), who relocated the foreshock and mainshock hypocenters using ocean bottom seismograph data deployed in the source area. The observation equation in our inversion is expressed as:

$$\begin{pmatrix} \mathbf{d}^{obs} \\ \mathbf{0} \end{pmatrix} = \begin{pmatrix} \mathbf{G} \\ \alpha\mathbf{S} \end{pmatrix} \mathbf{a}, \tag{1}$$

where $\mathbf{d}^{obs}$ is the vector of the observed tsunami waveforms, **G** is a matrix composed of the tsunami Green's functions, **S** is a matrix representing the smoothing constraint, and **a** is the vector of unknown parameters describing the amount of slip on the fault, which is being estimated. In this study, the goodness of the waveform fitting can be measured by a variance reduction (VR), defined as:

$$VR = \left(1 - \frac{\sum_{k=1}^{N} \left(d_k^{obs} - d_k^{calc} \right)^2}{\sum_{k=1}^{N} \left(d_k^{obs} \right)^2} \right) \times 100 \ (\%) , \tag{2}$$

where d_k^{obs} and d_k^{calc} are the k-th data of observed and calculated waveforms, respectively, and N is the number of data used for the inversion. In the inversion, we applied a non-negative least squares inversion (Lawson and Hanson, 1978) because negative (normal-faulting) slips are unlikely to happen on the fault during the two foreshocks. We empirically determined the weight of the smoothing constraint as $\alpha = 10$ by inspecting the trade-off curve between α and the VR (Figure S2) to avoid both excessive fitting and over-smoothing due to small and large α, respectively.

The tsunami Green's functions were calculated as waveforms caused by vertical seafloor displacement associated with the rupture of a small subfault placed along the plate boundary fault. Seafloor displacement was calculated using the equation by Okada (1992). The initial sea-surface height distribution was obtained by applying the depth filter, introduced by Saito and Furumura (2009), to the seafloor vertical deformation, which spatially smooths seafloor deformation. For the filtering, we assumed a constant water depth of 2 km, which is equal to the depth around the epicenters.

Tsunami waveforms were calculated based on a linear long-wave equation expressed in the local Cartesian coordinate system (e.g., Satake, 2002; Saito et al., 2014). In the calculation, we assumed that the slip of all the subfaults began at the same time and the slip duration was 10 s based on the GCMT solution. As bathymetry data, we resampled ETOPO1 (Amante and Eakins, 2009) into 2 km × 2 km gridded data. The time step interval of the calculation was 1 s. The pressure offset due to seafloor vertical deformation was taken into account according to a method devised by Tsushima et al. (2012) by subtracting the calculated vertical seafloor deformation from the calculated sea surface fluctuation at the point of the OBPG stations. After the tsunami calculation, we took the 60 s moving average and applied the low-pass filter, as for the observed pressure data.

One of the inputs to the model is the geometry of the plate boundary fault on which the two foreshocks ruptured. We assumed that the plate boundary fault can be approximated by a planar fault and took the dip and strike angles of the Global Centroid Moment Tensor (GCMT) solution for foreshock #1 (dip = 12° and strike = 189°) as those of the planar plate boundary fault. The assumed dip angle is consistent with the plate boundary model presented by Ito et al. (2005) based on active seismic exploration. Because the assumed strike direction matches that of the trench axis in this region, it is a good approximation of the local strike of the fault. We set the fault depth by referring to the model by Ito et al. (2005). Subfaults 20 km × 20 km in the dip and strike directions were distributed along the modeled plate boundary fault in the range spanning the area covering the epicenters of the relevant earthquakes and OBPG stations (120 km × 120 km, Figures 2 and 3).

In the inversion, we assumed the rake angle of slip on the subfault as a given constant from the GCMT solution for foreshock #1 (78°), for both foreshocks #1 and #2, after inspecting if the given rake angle is representative of those of interplate earthquakes in this area. We chose 65 interplate earthquakes (Mw > 6.0) having a strike of 170–210°, a dip of 0–45°, and a rake of 40–120°, according to the GCMT catalogue from 1 Jan. 2000 to 31 Dec. 2015, located in the region (37.5–39.5°N and 142–144°E). The average of their rake angles was 79.2 ± 2.0°, which is consistent with that of the GMT solution for foreshock #1 (78°).

4. Results

Figure 2 shows the result of the coseismic slip inversion for foreshock #1. The maximum slip is 1.23 m at the subfault marked by a thick green square in Figure 2a. The slip amounts in three subfaults adjacent to the maximum slip subfault are almost as large as the peak slip, that is 1.0, 0.96, and 0.95 m. Of the total slip, 74% is concentrated on these four subfaults, forming an area 40 km × 40 km northwest of the epicenter (the four subfaults are marked by a solid square in Figure 2a). The next two largest slips are 0.40 and 0.39 m, less than half the maximum slip, which are located north of the subfault with the largest slip and beneath P09, respectively. The spatial extent of the uplifted area of the initial sea-surface height expected from the fault slip model is consistent with the estimated source dimension based on the duration of tsunami pulses (~60 km). The obtained slip model explains the observed waveforms very well, and we obtained a VR of 86% for the foreshock #1 model.

Figure 3 shows the result of the coseismic slip inversion for foreshock #2. Large slip was concentrated on the two subfaults to the north and northwest of the epicenter (marked by solid rectangle in Figure 3a). The largest slip, 0.27 m, was obtained for the subfault beneath P09 (marked by a thick green square) and the second largest slip (0.17 m) was obtained for the subfault beneath P08. The slip amount on these two subfaults constitutes 57% of the total slip. The next largest slip amounts of 0.09, 0.07, and 0.05 m, less than half of that on the two subfaults, were estimated at three subfaults near the two large-slip subfaults; two were located to the south and one to the northeast. The spatial extent of the initial sea surface uplifted area expected from the fault slip model is almost consistent with the source size estimated from the tsunami pulse width, ~40 km. The calculated waveforms explain the observed waveforms well, and the VR was 76%.

Although we did not include the records obtained at TM1 and TM2 in the inversion, it would be worthwhile to see if the source models are consistent with these records. In both foreshocks, the coseismic slip models mostly explain the arrival times and peak amplitudes (Figure S3). It appears that a long-term drift remaining in the observed records accounts for the waveform misfits. Static offsets of ~5 hPa can be identified in the data of foreshock #1, but the seafloor vertical displacement of ~5 cm at the sites ~100 km away from the source is not probable. The amounts of the apparent offsets are comparable to the expected noise level in the records of TM1 and TM2 reported by

Inazu and Hino (2010). The higher noise level is another reason we did not include these data in the fault modeling.

Concentration of large, more than a half of the peak value, slips within small areas adjacent to the epicenter is a common feature of the obtained source models. In order to confirm the reliability of those large slips and also the significance of the smaller slips surrounding them, we carried out a test by performing different sets of inversion analyses. In the trial inversions, we used a larger model space along the trench (160 km instead of 120 km) and a longer time window (30 min instead of 20 min). Inversions with TM1 and TM2 data were also made. Further, inversions without a non-negative constraint were performed. In total, we carried out sixteen sets of inversions for each foreshock. The results of the test inversions are shown in Figures S4 and S5. The locations of large slip patches near the epicenters were consistently estimated throughout the different trials. However, the slip distributions in the margins are considerably different from one another, indicating less reliability of the solution there. To identify the region of reliable slip amount, we calculated the average and standard deviation of the slip amounts on subfaults from the results of additional inversions (Figure S6). Note that the averages and standard deviations for the 12 subfaults in the northern part of the model space are obtained from the results with larger model space, but those in the other subfaults are from all the inversion results. From this test, it is concluded that the characteristics of the source models explained earlier in this section is robustly estimated.

It is possible that slip over a small area has spread to a larger area because of smearing by the smoothing constraint imposed in the slip inversion. By taking these spreading effects into account, the subfaults with significant amounts of slip can be interpreted as the main rupture areas of the two foreshocks. In order to assess the spatial resolution of the inversion analysis, especially in the possible coseismic slip areas, we performed a recovery test (Figure S7). In the test, we gave slips of 1 m to subfaults where the large slip amounts were estimated, then the tsunami waveforms calculated from the given slip models were inverted for slip distributions. All the settings of the inversion analysis were the same as those in the inversion of the observation data. The test results demonstrate how well the amount of slip in the given rupture zone is recovered and how much slip leaks into the surrounding cells. The slip patterns of the test results (Figure S7) closely resemble those inverted from the observed data (Figures 2 and 3) and those of the averaged slip distribution (Figures S4 and S5). The results of the recovery test show that more than ~70% of the given slip was recovered.

We also attempted to confirm whether only the significant slip could explain the observed tsunami waveforms. First, we calculated tsunamis only from the outstanding slip area, keeping the amount of slip at subfaults the same as that estimated by the inversion analyses (Figure 4, blue traces). Although the arrival times and the pulse width of the tsunamis are well reproduced, the amplitudes and offset amounts are significantly smaller than those of the observed waveforms, producing smaller VR values, 66% and 72% for foreshocks #1 and #2, respectively. Then, we corrected the slip amounts in the main rupture areas, taking into account the slip reduction rates obtained by the recovery tests, in order to recalculate tsunami waveforms (Figure 4, red traces). The corrected slip amount $D_{corrected}$ is expressed as:

$$D_{corrected} = D_{estimaed} \times \frac{S_{given}}{S_{recovered}}, \quad (3)$$

where $D_{estimated}$ denotes the estimated slip amount in the inversion, and S_{given} and $S_{recovered}$ are the given slip amount (=1 m) and recovered slip amount on each subfault in the recovery test, respectively. The VRs are improved to 80% and 76% for foreshocks #1 and #2, respectively. Most of the characteristics of the observed waveforms are well modeled.

Based on these assessments, we define the subfaults with slips larger than half of the maximum slip as the main rupture area. The main rupture area of foreshock #1 is a square 40 km × 40 km located northwest of the epicenter, and that of foreshock #2 is a rectangular area 20 km long by 40 km wide. After correction with the recovery rates, the amounts of maximum slip are 1.3 m and 0.3 m, average slip of the main rupture areas are 1.2 m and 0.3 m, and seismic moments released from the main rupture areas are 7.6×10^{19} Nm (Mw 7.2) and 9.0×10^{18} Nm (Mw 6.6) for foreshocks #1 and #2, respectively, assuming a rigidity of 40 GPa. The good agreement between waveforms calculated from the single main rupture models indicates that the estimated location and spatial extent of the main rupture areas are reasonably constrained.

5. Discussion

5.1 Comparison with previous studies on foreshock sequence

We compare the main rupture areas of foreshocks #1 and #2 with the coseismic and postseismic slip distributions of foreshock #1 by Ohta et al. (2011) in Figure 5. The location and spatial extent of the main rupture area of foreshock #1 estimated in this study (red rectangle) agrees well with the coseismic slip distribution in Ohta et al. (2012) (yellow contours). Shao et al. (2011) and Gusman et al. (2012) also indicated that the coseismic slip of foreshock #1 is concentrated on the fault northwest of its epicenter, although the estimated sizes of the rupture area are wider than our results, possibly because of the spatial resolution limitation in the data they used. The near-field tsunami records used in this study significantly improved the source model, enabling a more detailed discussion of the relationship between the slip regions of other major events, the postseismic slip of foreshock #1, and the coseismic slip of foreshock #2.

The main rupture area of foreshock #2 (blue rectangle) does not overlap with that of foreshock #1, and is located between foreshock #1 and the mainshock epicenters. The postseismic slip area estimated by Ohta et al. (2012) is located southeast of the main rupture area of foreshock #1 and east of that of foreshock #2 (blue contours). The main rupture area of foreshock #1 does not overlap with the peak of the postseismic slip area, whereas that of foreshock #2 partially overlaps. Although Ohta et al. (2012) removed the clear coseismic displacement from the P09 data, they could not distinguish the coseismic deformation associated with foreshock #2 from that due to postseismic slip. This could explain the partial overlap between the main rupture area of foreshock #2 and the area of aseismic slip after foreshock #1.

In Figure 5, the epicenters of foreshocks relocated by Suzuki et al. (2012) are also plotted. The epicenters of earthquakes occurring immediately after foreshock #1 and before foreshock #2, and those after foreshock #2 until the mainshock on March 11 are plotted with open and solid symbols, respectively. We can point out that most foreshock epicenters, regardless of their timing, are distributed outside of the main rupture area of foreshock #1. If we regard the intense seismicity after foreshock #1 as aftershocks, this complementary relationship is the same as that between the mainshock rupture zone and the aftershock distribution commonly found for many large earthquakes (e.g., Hartzell, 1989; Hirata et al., 1996; Shinohara et al., 2004). We further note that the seismicity is concentrated along the updip and southern sides of the main rupture zone of foreshock #1, but not on the downdip and northern sides. In the southern part of the main rupture area of foreshock #1, most of the earthquakes occurred after foreshock #2 (solid circles). Notably, no aftershocks are identified before foreshock #2 to the south of the main rupture area of foreshock #2, suggesting that secondary aftershocks migrated further south after foreshock #2.

We interpret the spatio-temporal relationship between the obtained source models and foreshock activity based on the idea suggested by previous studies (e.g. Ando and Imanishi, 2011; Kato et al. 2012; Ohta et al., 2012), in which the series of foreshock activity is interpreted as the consequence of propagating aseismic slip, as follows. Following foreshock #1, its postseismic slip migrated to the east and south, causing intense seismicity. Foreshock #2, one of the earthquakes triggered by aseismic slip that propagated southward from foreshock #1, advanced the propagation of aseismic slip further to the south, becoming postseismic slip, causing the increasing seismicity along the southern rim of the foreshock #2 rupture. This aseismic slip could have triggered the initial rupture of the mainshock.

5.2 Stress drops of the two foreshocks

We calculated the stress drop $\Delta\sigma$ associated with the two foreshocks from the source areas and slip amounts estimated here, based on the conventional relationship (e.g., Kanamori and Anderson, 1975) expressed as:

$$\Delta\sigma = c\,\mu D / \sqrt{S}\ , \tag{4}$$

where c is constant and μ, D, and S are the shear modulus (=40 GPa), average slip, and size of the rupture area, respectively. In this calculation, Poisson's ratio is assumed to be 0.25, and we obtain c = $8/3\pi$ from Kanamori and Anderson (1975). In the calculation, we used the average slip amounts of the modified main rupture model (1.2 m and 0.3 m for foreshocks #1 and #2, respectively). The fault sizes are 1600 km^2 for foreshock #1 and 800 km^2 for foreshock #2, which are also taken from the size of the main rupture area.

The obtained stress drop is $\Delta\sigma$ =1.0 MPa for foreshock #1 and 0.3 MPa for foreshock #2. For foreshock #1, this is comparable to that estimated by Shao et al. (2011). Shao et al. (2011) suggested that foreshock #1 is a typical M~7 earthquake in terms of the stress drop calculation. The expected size of the main slip area of typical Mw 7.2 earthquakes is ~1400 km^2, if we apply the scaling relationship proposed by Blaser et al. (2010). This is similar to that of the main rupture area of foreshock #1 in our model. Nevertheless, the scaling relationship predicts a fault area of ~330 km^2 for a Mw 6.6 earthquake, which is smaller than that of our rupture model for foreshock #2. Therefore, it appears that foreshock #2 has a disproportionally larger rupture area than typical earthquakes, and this large rupture size is the reason for its small stress drop.

However, it could be of concern whether or not the grid size and layout of our inversion are appropriate for correctly estimating the rupture size of the smaller foreshock #2. Here, we carried out a test to confirm whether the size of the main rupture area of foreshock #2 is significantly larger than the typical rupture size. In the test, we assumed that the rupture of foreshock #2 could be expressed as one subfault (400 km^2), which is similar to the typical fault size expected from the scaling relationship. The slip amount was assumed to be 0.5 m, so that the seismic moment was equivalent to that of the preferred model. This trial model yields a stress drop of ~0.90 MPa, which is almost identical to that of foreshock #1.

As the first trial, we set the fault so that its center matched that of our preferred model (blue hatched area in Figure 6a) and calculated the tsunami waveforms to compare with the observed waveforms (model A, blue square in Figure 6a). The calculated pressure offset change at P09 is much larger than the observed one (blue traces in Figure 6b) and the VR is very low (24%). Next, the fault was shifted by 10 km to the south along the strike (model B, red square in Figure 6a). This model mostly explains the characteristics of the observed waveforms (red traces in Figure 6b), but the duration of the main tsunami pulses is shorter than the observations, as clearly seen in the waveforms at P02 and P06. The calculated VR is 70%, which is smaller than that obtained from the preferred model (76%). After the test, it is probable that the observed tsunami waveforms do not conform with the fault rupture according to a stress drop comparable to that of foreshock #1.

Some studies reported that the stress drops of aftershocks are smaller than their mainshocks (Somei et al., 2014; Nakano et al., 2015). Although no specific physical reasons have been given, the stress drop difference between foreshocks #1 and #2 may be a manifestation of the proposed mainshock–aftershock relationship. A possible reason is the stress evolution or strength reduction associated with processes causing aftershocks. If the process after foreshock #1 involves pore fluid diffusion, it could reduce the strength along the plate boundary fault surrounding the ruptured area (e.g., Nur and Booker, 1972; Bell and Nur, 1978; Bosl and Nur, 2002). Frictional strength on the fault can be reduced under the high loading rate (e.g., Cao and Aki, 1986; Karner and Marone, 2000). Since it is expected that aseismic slip after foreshock #1 increased the loading rate to the locked patch of foreshock #2, it is probable that the smaller stress drop of foreshock #2 reflects the strength reduction caused by the postseismic slip following foreshock #1. However, it also has to be pointed out that the strength can vary spatially along the fault, and the stress drop difference might be simply a consequence of the inhomogeneous distribution of strength.

5.3 Comparison with M 7.0 event in 1981

In the area of foreshock activity preceding the 2011 Tohoku-Oki earthquake, an earthquake of M 7.0 occurred on 19 January 1981. The 1981 earthquake was followed by clear aftershock seismicity, including several earthquakes of M~6, similar to the seismicity after foreshock #1. Ando and Imanishi (2011) pointed out a similarity between the 1981 seismicity and the foreshock sequence in 2011 based on the epicenter distribution. In this section, we explore the relationship between the rupture areas of the two M 7 class earthquakes activating the seismic sequences.

The finite fault model of the 1981 earthquake was derived from the terrestrial strong motion seismograms by Yamanaka and Kikuchi (2004). Hatori (1981) examined the tsunami generated by the 1981 earthquake at coastal tide stations to estimate the spatial extent of the tsunami source. Both results show good agreement with the rupture area of foreshock #1 in 2011 obtained in this study (Figure 7), suggesting that foreshock #1 was a recurrent rupture of the fault patch ruptured in 1981. However, there are notable discordances; a ~30 km difference in epicenter locations and the larger size of the 1981 source estimated by either seismographs or tsunami records, in spite of its smaller magnitude. These differences could arise from the different resolutions between the previous studies, using old and remote data, and this study, based on near field observations.

We examined the difference between the source models of the 1981 earthquake and foreshock #1 based on a comparison of coastal tsunami records, since the records are supposed to be comparable in quality for both earthquakes. In the comparison, we did not perform a waveform inversion for the source models because of the low signal-to-noise ratio of records in 1981. Instead, we compared the travel times (time difference between the arrival times and the origin times according to the JMA catalogue) and amplitudes of the first up-going tsunami wave at coastal stations, summarized by Hatori (1981) for the 1981 event. For foreshock #1 in 2011, we used the observed coastal tsunami time series provided by the Japan Meteorological Agency (JMA, http://www.jma.go.jp/jma/press/1103/10a/kaisetsu201103100820.pdf, in Japanese). The result of the comparison is shown in Table 2. The amplitudes of the 1981 event are about half those of foreshock #1, consistent with the smaller magnitude of the 1981 earthquake. The differences in arrival times never exceed 5 min at all stations, although the travel times of the 1981 earthquake tsunami are shorter by a few minutes in some stations. A few minutes difference in arrival times can be approximated as a distance of ~15–25 km, based on the estimated tsunami wave speed

(~140 m/s) in this region. Based on comparisons of travel times, the location of the tsunami source of the 1981 event is almost identical to that of foreshock #1, but may be shifted slightly landward to explain the earlier arrivals of the 1981 tsunami.

We carried out another evaluation based on the tsunami numerical calculations to discuss the difference in coastal tsunami waveforms characteristics between the 1981 and 2011 earthquakes in more detail. We calculated the coastal tsunami waveforms using the long-wave equation. For the source model, we assumed a rectangular fault on the plate boundary with length, width, and slip of 40 km, 20 km, and 0.7 m, respectively. These values were set based on the scaling law of Blaser et al. (2010) for a typical M 7.0 earthquake. In Figure 8, the calculated tsunami waveforms for foreshock #1 and for the 1981 earthquake are compared. Taking the earlier tsunami arrivals at the coast into account, we set a model composed of two subfaults corresponding to the deeper half of the foreshock #1 rupture area for the 1981 earthquake (orange rectangle in Figure 8a), whereas our preferred model for foreshock #1 in 2011 is composed of four subfaults (red hatched square in Figure 8a). The maximum uplift and subsidence expected from the 1981 fault model are 13.5 cm and 6.7 cm, respectively, which are less than half of those for foreshock #1.

We compared the travel times and amplitudes as we did for the observed records. In Figures 8b and 8c, we mark, using allows, the onsets of up-going waves, defined as the time when the uplift amplitude exceeds 1 cm,. The onset times are very close at all stations, but slightly earlier arrivals can be seen for the 1981 tsunami than for foreshock #1, as we found when comparing the observed waveforms. The calculated amplitudes of the initial waves of the 1981 event are about half of those for foreshock #1, and we therefore regard that the observed characteristics are well reproduced by this modeling. It is notable that the epicenter of the 1981 earthquake coincides with the up-dip edge of the modeled fault, as for the epicenter of foreshock #1, suggesting that the rupture propagated down-dip in both events.

We also calculated tsunamis by shifting the 1981 fault in the dip direction to determine how the travel time differences are sensitive to the source locations (blue and green rectangles in Figure 8a). The arrival times of the first up-going waves are significantly different from those of foreshock #1 or those of the 1981 model, assuming the down-dip half of the 2011 fault. It can be concluded that the 1981 fault must overlap the rupture area of foreshock #1 in order to explain the observed tsunami waveforms. We speculate that foreshock #1 broke the fault patch ruptured in 1981 again in 2011, but generated further slip on the up-dip side of the 1981 patch and therefore became a larger earthquake.

It is beyond the scope of this study to determine why the 1981 earthquake was not followed by a Mw 9 megathrust earthquake while foreshock #1 was, even though these earthquakes are considered to be ruptures of an identical fault patch. The postseismic deformation associated with the 1981 earthquake was observed by a tiltmeter placed at station Esashi (International Latitude Observatory of Mizusawa, 1981). The observation strongly suggests the 1981 earthquake was followed by substantial aseismic afterslip, but the data quality does not allow quantitative comparison with the postseismic process following foreshock #1 in 2011. Sato et al. (2013) argued that a series of large ($M > \sim 6$) earthquakes near the epicenters of the 2011 mainshock or of foreshock #1 facilitated the occurrence of the Tohoku-Oki earthquake by weakening interplate coupling. Since the

1981 earthquake was not preceded by pronounced activity near its epicenter, the difference between the two earthquakes in 2011 and 1981, with or without additional rupture of the up-dip side, might be related to the difference in the stress condition and might provide clues for understanding the processes leading to generation of the very large 2011 earthquake.

6. Conclusion

Based on the analysis of tsunami waveforms observed by OBPGs deployed just above the focal area, we developed fault models for the largest and second largest foreshocks (foreshocks #1 and #2, respectively) of the 2011 Tohoku-Oki earthquake. The use of the near-field tsunami records helped us to obtain good spatial resolution of the source model, especially the fault model of foreshock #2, which had never been obtained, because of its small size for finite source modeling. Our result showed that the main rupture areas of foreshocks #1 and #2 did not overlap. From comparison with the spatio-temporal evolution of small earthquake activity after foreshock #2, we suggest that foreshock #2 was triggered by postseismic slip following foreshock #1, and aseismic slip propagated further south, towards the mainshock epicenter, after foreshock #2. The stress drop of foreshock #2 seems to be smaller than that of foreshock #1, which is likely associated with the strength reduction along the plate interface under aseismic slip with intense seismicity. Foreshock #1 is likely to have been a re-rupture of the fault patch ruptured during the M 7.0 earthquake in 1981, but ruptured a wider area that included the up-dip side of the 1981 source.

Acknowledgements

The authors thank the Earthquake Research Institute of the University of Tokyo for the use of tsunami data recorded by the cabled ocean-bottom pressure sensors of the observatory off Kamaishi. The coastal tide waveforms used in this study were recorded by the Japan Meteorological Agency (JMA), the Japan Coast Guard (JCG), the Ports and Harbors Bureau under the Ministry of Land, Infrastructure, Transport, and Tourism (MLIT), and the Port and Airport Research Institute (PARI). The authors wish to thank Dr. Tatsuhiko Saito of the National Research Institute for Earth Science and Disaster Prevention (NIED), for the Fortran code to calculate the tsunamis, as well as helpful comments. The authors deeply thank two anonymous reviewers for constructive comments on the manuscript. This study was supported by the research project "Research concerning Interaction between the Tokai, Tonankai, and Nankai earthquakes" of the Ministry of Education, Culture, Sports, Science and Technology, and by JSPS KAKENHI (A) 20244070 and 26000002. The figures in this paper were prepared using Generic Mapping Tools (GMT) (Wessel and Smith, 1998). The authors used the English language editing service Editage (www.editage.jp).

References

Amante, C., Eakins, B., 2009. ETOPO1 1 arc-minute global relief model: procedures, data sources and analysis, in NOAA Tech. Memo. NESDIS NGCD-24, 19 pp., Natl. Geophys. Data Center, NOAA, Boulder, Colo.

Ando, R., Imanishi, K., 2011. Possibility of Mw 9.0 mainshock triggered by diffusional propagation of after-slip from Mw 7.3 foreshock. Earth Planets Space 63, 767–771, doi: 10.5047/eps.2011.05.016.

Bell, M. L., Nur, A., 1978. Strength changes due to reservoir-induced pore pressure and stresses and application to Lake Oroville. J. Geophys. Res. 83, 4469–4483, doi: 10.1029/JB083iB09p04469.

Blaser, L., Krüger, F., Ohrnberger, M., Scherbaum, F., 2010. Scaling relations of earthquake source parameter estimates with special focus on subduction environment. Bull. Seism. Soc. Am. 100, 2914–2926, doi: 10.1785/0120100111.

Bosl, W. J., Nur, A., 2002. Aftershocks and pore fluid diffusion following the 1992 Landers earthquake. J. Geophys. Res. 107, 2366, doi: 10.1029/2001JB000155.

Cao, T., Aki, K., 1986. Effect of slip rate on stress drop. Pure Appl. Geophys. 124, 515–529, doi: 10.1007/BF00877214.

Gusman, A. R., Fukuoka, M., Tanioka, Y., Sakai, S., 2013. Effect of the largest foreshock (Mw 7.3) on triggering the 2011 Tohoku earthquake (Mw 9.0). Geophys. Res. Lett. 40, 497–500, doi: 10.1002/grl.50153.

Hartzell, S., 1989, Comparison of seismic waveform inversion results for the rupture history of a finite fault: application to the 1986 North Palm Springs, California, Earthquake. J. Geophys. Res. 96, 7515–7534, doi: 10.1029/JB094iB06p07515.

Hatori, T., 1981. Tsunami sources in the Sanriku region in 1979 and 1981, Northeastern Japan – seismic gap off Miyagi. Bull. Earthq. Res. Inst. 56, 629–640, http://repository.dl.itc.u-tokyo.ac.jp/dspace/bitstream/2261/12823/1/ji0564001.pdf (accessed 16.9.9).

Hino, R., Tanioka, Y., Kanazawa, T., Sakai, S., Nishino, M., Suyehiro, K., 2001. Micro-tsunami from a local interplate earthquake detected by cabled offshore tsunami observation in northeastern Japan. Geophys. Res. Lett. 28, 3533–3536, doi: 10.1029/2001GL013297.

Hino, R., Inazu, D., Ohta, Y., Ito, Y., Suzuki, S., Iinuma, T., Osada, Y., Kido, M., Fujimoto, H., Kaneda, Y., 2014. Was the 2011 Tohoku-Oki earthquake preceded by aseismic preslip? Examination of seafloor vertical deformation data near the epicenter. Mar. Geophys. Res. 35, 181–190, doi: 10.1007/s11001-013-9208-2.

Hirata, N., Ohmi, S., Sakai, S., Katsumata, K., Matsumoto, S., Takanami, T., Yamamoto, A., Iidaka, T., Urabe, T., Sekine, M., Ooida, T., Yamazaki, F., Katao, H., Umeda, Y., Nakamura, M., Seto, T., Matsushima, T., Shimizu, H., Japanese University Group for the Urgent Joint Observation for the 1995 Hyogo-ken Nanbu Earthquake, 1996. Urgent joint observation of aftershocks of the 1995 Hyogo-ken Nanbu earthquake. J. Phys. Earth 44, 317–328, doi: 0.4294/jpe1952.44.317.

Ide, S., Baltay, A., Beroza, G. C., 2011. Shallow dynamic overshoot and energetic deep rupture in the 2011 Mw 9.0 Tohoku-Oki earthquake. Science 332, 1426, doi: 10.1126/science.1207020.

Iinuma, T., Hino, R., Kido, M., Inazu, D., Osada, Y., Ito, Y., Ohzono, M., Tsushima, H., Suzuki, S., Fujimoto, H., Miura, S., 2012. Coseismic slip distribution of the 2011 off the Pacific Coast of Tohoku Earthquake (M9.0) refined by means of seafloor geodetic data. J. Geophys. Res. 117, B07409, doi: 10.1029/2012JB009186.

Inazu, D., Hino, R., 2011. Temperature correction and usefulness of ocean bottom pressure data from cabled seafloor observatories around Japan for analyses of tsunamis, ocean tides, and low-frequency geophysical phenomena. Earth Planets Space 63, 1133–1149, doi: 10.5047/eps.2011.07.014.

Inazu, D., Saito, T., 2014. Two subevents across the Japan Trench during the 7 December 2012 off Tohoku earthquake (Mw 7.3) inferred from offshore tsunami records. J. Geophys. Res. 119, 5800–5813, doi: 10.1002/2013JB010892.

International Latitude Observatory of Mizusawa, 1981. Observations of crustal movements at the Esshi earth tide station (in Japanese). Rep. Coordinating Committee for Earthquake Prediction. 26, 33–37, http://cais.gsi.go.jp/YOCHIREN/report/kaihou26/02_03.pdf (accessed 16.9.9).

Ito, A., Fujie, G., Miura, S., Kodaira, S., Kaneda, Y., Hino, R., 2005. Bending of the subducting oceanic plate and its implication for rupture propagation of large interplate earthquakes off Miyagi, Japan, in the Japan Trench subduction zone. Geophys. Res. Lett. 32, L05310, doi: 10.1029/2004GL022307.

Kanamori, H., Anderson, D. L., 1975. Theoretical basis of some empirical relations in seismology. Bull. Seismol. Soc. Am. 65, 1073–1095.

Kanazawa, T., Hasegawa, A., 1997. Ocean-bottom observatory for earthquakes and tsunami off Sanriku, north-east Japan using submarine cable. in: H. Utado et al. (Eds.), Proceedings of International Workshop on Scientific Use of Submarine Cables, pp. 208–209, Comm. for Sci. Use of Submarine Cables, Okinawa, Japan.

Karner, S. L., Marone, C., 2000. Effects of loading rate and normal stress on stress drop and stick-slip recurrence interval, in: Rundle, J. B., Turcotte, D. L., Klein, W. (Eds.), Geocomplexity and the Physics of Earthquakes. American Geophysical Union, Washington, D. C., pp. 187–198.

Kato, A., Obara, K., Igarashi, T., Tsuruoka, H., Nakagawa, S., Hirata, N., 2012. Propagation of slow slip leading up to the 2011 Mw 9.0 Tohoku-Oki earthquake. Science 335, 705–708, doi: 10.1126/science.1215141.

Kubota, T., Hino, R., Inazu, D., Ito, Y., Iinuma, T., 2015. Complicated rupture process of the Mw 7.0 intraslab strike-slip earthquake in the Tohoku region on 10 July 2011 revealed by near-field pressure records. Geophys. Res. Lett. 42, 9733–9739, doi: 10.1002/2015GL066101.

Matsumoto, K., Takanezawa, T., Ooe, M., 2000. Ocean tide models developed by assimilating TOPEX/POSEIDON altimeter data into hydrodynamical model: a global model and a regional model around Japan. J. Oceanogr. 56, 567–581, doi: 10.1023/A:1011157212596.

Nakano, K., Matsushima, S., Kawase, H., 2015. Statistical properties of strong ground motions from the generalized spectral inversion of data observed by K-NET, KiK-net, and the JMA Shindokei network in Japan. Bull. Seismol. Soc. Am. 105, 2662–2680, doi: 10.1785/0120140349.

Nur. A, Booker, J. R., 1972. Aftershocks caused by pore fluid flow? Science 175, 885–887, doi: 10.1126/science.175.4024.885.

Ohta, Y., Hino, R., Inazu, D., Ohzono, M., Ito, Y., Mishina, M., Iinuma, T., Nakajima, J., Osada, Y., Suzuki, K., Fujimoto, H., Tachibana, K., Demachi, T., Miura, S.,

2012. Geodetic constraints on afterslip characteristics following the March 9, 2011, Sanriku-oki earthquake, Japan. Geophys. Res. Lett. 39, L16304, doi: 10.1029/2012GL052430.

Okada, Y., 1992. Internal deformation due to shear and tensile faults in a half-space, Bull. Seismol. Soc. Am. 82, 1018–1040.

Ozawa, S., Nishimura, T., Suito, H., Kobayashi, T., Tobita, M., Imakiire, T., 2011. Coseismic and postseismic slip of the 2011 magnitude-9 Tohoku-Oki earthquake. Nature 475, 373–376, doi: 10.1038/nature10227.

Saito, M., 1978. An automatic design algorithm for band selective recursive digital filters (in Japanese). Butsuri Tanko 31, 112–135.

Saito, T., Furumura, T., 2009. Three-dimensional tsunami generation simulation due to sea-bottom deformation and its interpretation based on the linear theory. Geophys. J. Int. 178, 877–888, doi: 10.1111/1365-246X.2009.04206.x.

Saito, T., Satake, K., Furumura, T., 2010. Tsunami waveform inversion including dispersive waves: the 2004 earthquake off Kii Peninsula, Japan. J. Geophys. Res. 115, B06303, doi: 10.1029/2009JB006884.

Saito, T., Ito, Y., Inazu, D., Hino, R., 2011. Tsunami source of the 2011 Tohoku-Oki earthquake, Japan: Inversion analysis based on dispersive tsunami simulations. Geophys. Res. Lett. 38, L00G19, doi: 10.1029/2011GL049089.

Saito, T., Inazu, D., Miyoshi, T., Hino, R., 2014. Dispersion and nonlinear effects in the 2011 Tohoku-Oki earthquake tsunami. J. Geopys. Res. 119, 5160–5180, doi: 10.1002/2014JC009971.

Satake, K., 2002. Tsunamis, in: Lee, W. H. K., Kanamori, H., Jennings, P. C., Kisslinger, C. (Eds.), International Handbook of Earthquake and Engineering Seismology, Int. Geophys. Academic Press, London. 81A, pp. 437–451.

Satake, K., Fujii, Y., Harada, T., Namegaya Y., 2013. Time and space distribution of coseismic slip of the 2011 Tohoku earthquake as inferred from tsunami waveform data. Bull. Seismol. Soc. Am. 103, 1473–1492, doi: 10.1785/0120120122.

Sato, T., Hiratsuka, S., Mori, J., 2013. Precursory Seismic Activity Surrounding the High-Slip Patches of the 2011 Mw 9.0 Tohoku-Oki Earthquake. Bull. Seism. Soc. Am. 103, 3104–3114, doi: 10.1785/0120130042.

Shao, G., Ji, C., Zhao, D., 2011. Rupture process of the 9 March, 2011 Mw 7.4 Sanriku-Oki, Japan earthquake constrained by jointly inverting teleseismic waveforms, strong motion data and GPS observations. Geophys. Res. Lett. 38, L00G20, doi: 10.1029/2011GL049164.

Shinohara, M., Yamada, T., Kanazawa, T., Hirata, N., Kaneda, Y., Takanami, T., Mikada, H., Suyehiro, K., Sakai, S., Watanabe, T., Uehira, K., Murai, Y., Takahashi, N., Nishino, M., Mochizuki, K., Sato, T., Araki, E., Hino, R., Uhira, K., Shiobara, H., Shimizu, H., 2004. Aftershock observation of the 2003 Tokachi-oki earthquake by using dense ocean bottom seismometer network. Earth Planets Space 56, 295–300, doi: 10.1186/BF03353054.

Simons, M., Minson, S. M., Sladen, A., Ortega, F., Jiang, J., Owen, S. E., Meng, L., Ampuero, J.-P., Wei, S., Chu, R., Helmberger, D. V., Kanamori, H., Hetland, E., Moore, A. W., Webb, F. H., 2011. The 2011 magnitude 9.0 Tohoku-Oki earthquake: mosaicking the megathrust from seconds to centuries. Science 332, 1421–1425, doi: 10.1126/science.1206731.

Somei, K., Asano, K., Iwata, T., Miyakoshi, K., 2014. Source scaling of inland crustal earthquake sequences in Japan using the S-wave coda spectral ratio method. Pure Appl. Geophys. 171, 2747–2766, doi: 10.1007/s00024-014-07774-2.

Suzuki, K., Hino, R., Ito, Y., Yamamoto, Y., Suzuki, S., Fujimoto, H., Shinohara, M., Abe, M., Kawaharada, Y., Hasegawa, Y., Kaneda Y., 2012. Seismicity near the hypocenter of the 2011 off the Pacific coast of Tohoku earthquake deduced by using ocean bottom seismographic data. Earth Planets Space 64, 1125–1135, doi: 10.5047/eps.2012.04.010.

Tanioka, Y., Hino, R., Hasegawa, Y., 2007. Slip distribution estimated from tsunami waveforms for the 2005 Miyagi-oki earthquake occurred on August 16 (in Japanese with English abstract). Zisin 2 59, 385-387.

Tsushima, H., Hino, R., Tanioka, Y., Imamura, F., Fujimoto, H., 2012. Tsunami waveform inversion incorporating permanent seafloor deformation and its application to tsunami forecasting. J. Geophys. Res. 117, B03311, doi: 10.1029/2011JB008877.

Wessel, P., Smith, W. H. F., 1998. New, improved version of generic mapping tools released. Eos Trans. AGU 79(47), 579, doi: 10.1029/98EO00426.

Yamanaka, Y., Kikuchi, M., 2004. Asperity map along the subduction zone in northeastern Japan inferred from regional seismic data. J. Geophys. Res. 109, B07307, doi: 10.1029/2003JB002683.

Table 1. Locations and observation periods of OBPGs

Station	Latitude [°N]	Longitude [°E]	Depth [m]	Operation (Month/Year)
GJT3[a]	38.2945	143.4814	3,293	Nov/2010–May/2011
P02[a]	38.5002	142.5016	1,104	June/2010–May/2011
P03[a]	38.1834	142.3998	1,052	June/2010–Sept/2011
P06[a]	38.6340	142.5838	1,254	June/2010–May/2011
P07[a]	38.0003	142.4488	1,059	Sept/2010–Sept/2011
P08[a]	38.2855	142.8330	1,418	Sept/2010–Sept/2011
P09[a]	38.2659	143.0006	1,556	June/2010–Sept/2011
TM1[b]	39.2330	142.7830	1,564	Continuous observation
TM2[b]	39.2528	142.4500	954	(Before March 11, 2011)

[a]Pop-up recovery OBPG identical to those used in Hino et al. (2014)

[b]Real-time cabled observation systems operated by Earthquake Research Institute (ERI) of the University of Tokyo (Kanazawa and Hasegawa, 1997)

Table 2. Travel times and amplitudes of initial waves of tsunami observed by coastal wave gauges.

Station	1981 Off-Miyagi		Foreshock #1		Agency[c]
	Travel time [min][a]	Amplitude [cm][a]	Travel time [min][b]	Amplitude [m][b]	
Hachinohe	62	3	65	0.1	JMA
Miyako	30	8	33	0.2	JMA
Kamaishi	26	23	28	0.4	JCG
Ofunato	26	20	26	0.6	JMA
Ayukawa	33	8	33	0.5	JMA
Sendai Port	68	4	69	0.2	PARI
Souma	60	3	65	0.2	GSI
Onahama	54	3	55	0.1	JMA

[a]Travel time and amplitude data from Hatori (1981).

[b]Travel time and amplitude read from waveforms of coastal wave gauges shown by JMA.

[c]JMA, JCG, PARI, and GSI are Japan Meteorological Agency, Japan Coast Guard, Port and Airport Research Institute, and Geospatial Information Authority of Japan, respectively.

Figure Captions

Figure 1. Location map of this study. Green inverted triangles denote location of offline OBPGs; black triangles are real-time cabled OBPGs. Stars and beach balls denote epicenter locations (Suzuki et al., 2012) and Global CMT mechanisms of foreshock #1 (red) and #2 (blue), and M9 mainshock (black), respectively. Gray contour lines show coseismic slip distribution of mainshock derived by Iinuma et al. (2012) with 10 m contour intervals. Topography data are from ETOPO-1.

Figure 2. (a) Estimated coseismic slip distribution of foreshock #1. Red and blue represent positive (reverse-faulting) and negative (normal-faulting) slip, respectively. Distribution of subfaults is shown by dashed line. Contours denote expected initial sea-surface height distribution calculated from the slip model with 10 cm intervals (solid and dashed lines are uplift and subsidence, respectively). Main rupture area is denoted thin black line, and subfault with the largest slip is denoted by thick green line. (b) Comparison of observed (gray) and synthesized waveforms based on slip model (red). Waveforms in white background area are used in the inversion.

Figure 3. (a) Estimated coseismic slip distribution of foreshock #2. Contours are in 2 cm intervals. (b) Comparison between observed and synthesized waveforms. See Figure 2 caption for detailed explanation.

Figure 4. Comparison of calculated tsunami waveforms assuming slip in the main rupture areas of (a) foreshock #1 and (b) #2. Observed waveforms are shown by gray line. Blue dashed lines and red solid lines show calculated waveforms with uncorrected and corrected slip amounts, respectively.

Figure 5. Main rupture areas of foreshock #1 and #2 and coseismic and postseismic slip distribution of foreshock #1 estimated by Ohta et al. (2012). Red and blue rectangles denote main rupture areas of foreshocks #1 and #2 estimated in this study, respectively. Orange contours indicate coseismic slip distribution of foreshock #1 of Ohta et al. (2012) with 0.5 m interval. Blue contours indicate postseismic slip distribution (Ohta et al., 2012) with 0.1 m interval. Open circles denote epicenters of aftershocks occurring between foreshocks #1 and #2; solid circles are epicenters of earthquakes occurring between foreshock #2 and mainshock. Epicenter locations are determined by Suzuki et al. (2012).

Figure 6. Result of the numerical test to evaluate size of foreshock #2 rupture. (a) Blue square represents fault model A, a 20×20 km^2 fault with a center location identical to main rupture area of foreshock #2, shown by blue hatched rectangle. Red square represents model B, with the same fault size but shifted south by 10 km. (b) Observed tsunami waveforms (gray) with calculated traces for model A (blue) and model B (red).

Figure 7. Main rupture area of foreshock #1 and source models of the 1981 Off-Miyagi earthquake (M7.0). Red square is main rupture area of foreshock #1 in 2011. Black

contours show initial sea surface height distribution from foreshock #1. Yellow shading indicates area with coseismic slip larger than 0.3 m for the 1981 earthquake (Yamanaka and Kikuchi, 2004). Green shading indicates tsunami source model of 1981 event (Hatori, 1981). Red and light gray stars are epicenters of foreshock #1 and mainshock, respectively, by Suzuki et al. (2012). Yellow star indicates epicenter of 1981 earthquake (JMA). Blue square indicates location of tiltmeter (Esashi) recording postseismic deformation of the 1981 earthquake.

Figure 8. Calculated tsunami waveforms at coastal stations from foreshock #1 and source models for 1981 earthquake. (a) Three fault models with different locations for 1981 earthquake. Orange rectangle is preferred model, corresponding to down-dip half of main rupture area of foreshock #1 (indicated by red hatched area). Green and blue rectangles are fault models located outside of rupture area of foreshock #1. Red and orange stars are epicenters of foreshock #1 and 1981 earthquake, respectively. Distribution of coastal tide stations is also shown. (b) Calculated tsunami waveforms from fault model of foreshock #1 (gray) and preferred model (red). Small arrows denote timings of onsets of tsunami waves. Arrow colors indicate the difference of assumed fault models, gray: foreshock #1, red: preferred 1981 earthquake model, green: model located landward of foreshock #1 fault, blue: model located trenchward of foreshock #1 fault. (c) Close-up of calculated tsunami waveform at Ofunato in time window shown by thick black bar in (b). Waveforms from models located landward and trenchward of foreshock #1 fault are shown by green and blue dashed lines, respectively. Other captions are the same as (b).

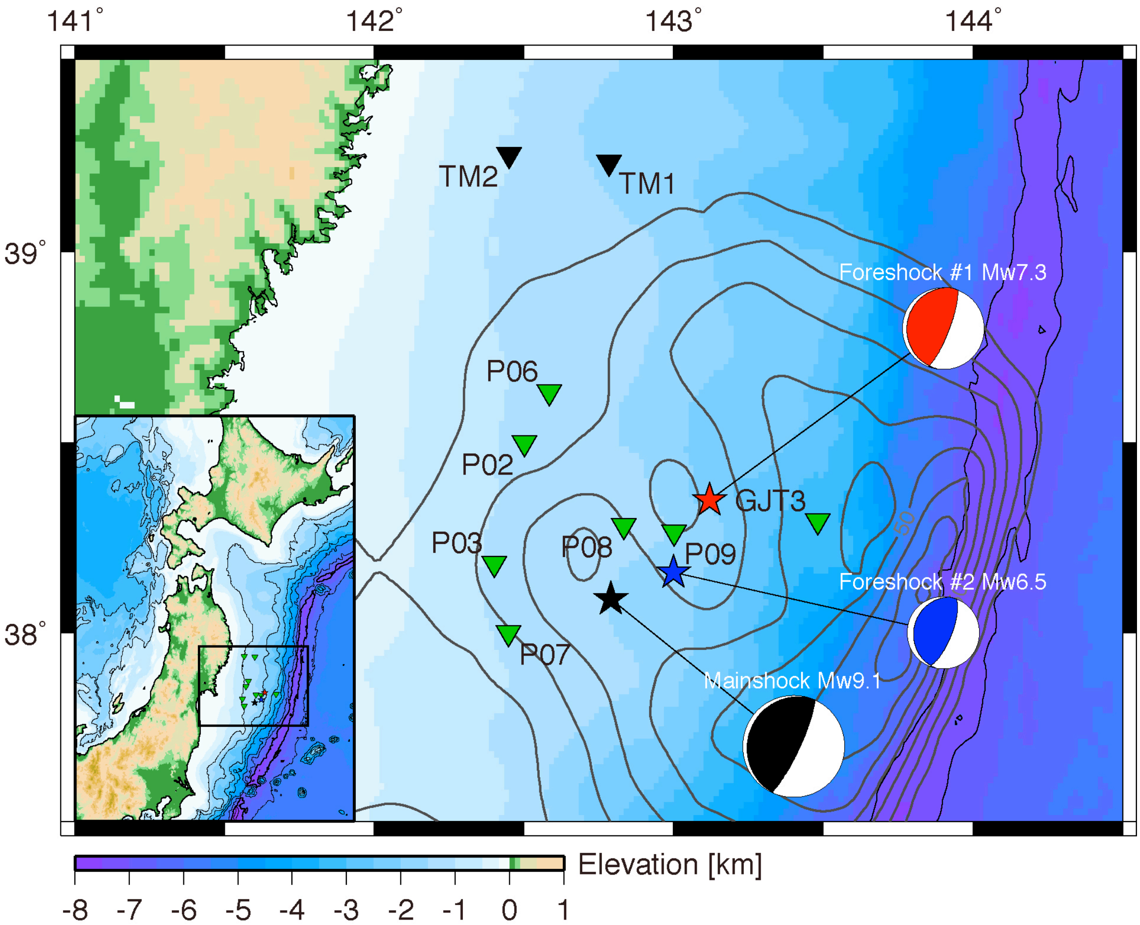
141°
142°
143°
144°
39°
38°
TM2
TM1
P06
P02
P03
P08
P09
GJT3
P07
Foreshock #1 Mw7.3
Foreshock #2 Mw6.5
Mainshock Mw9.1
50
Elevation [km]
-8 -7 -6 -5 -4 -3 -2 -1 0 1

Figure 1

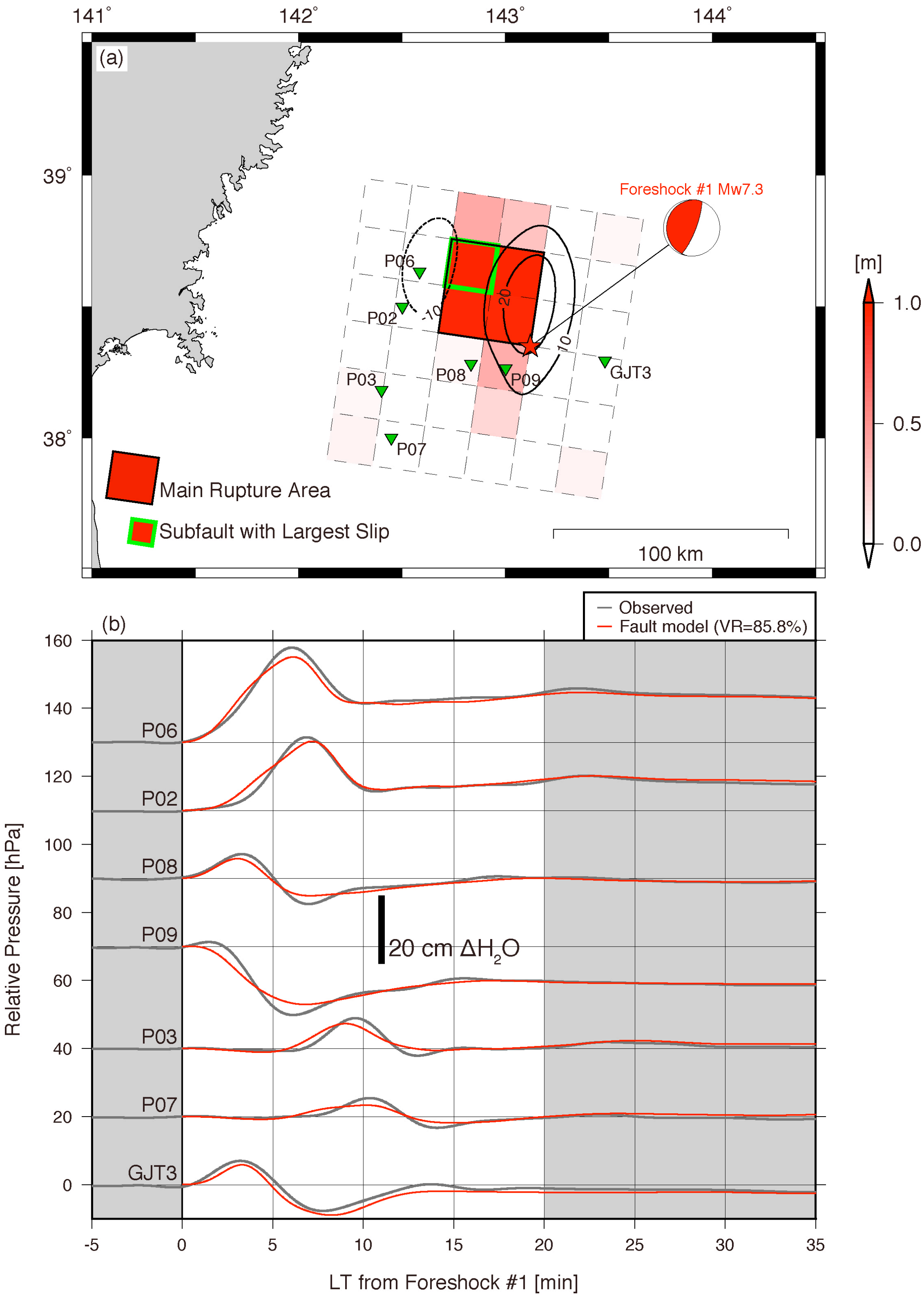
(a)
141°
142°
143°
144°
39°
38°
Foreshock #1 Mw7.3
P06
P02
P03
P07
P08
P09
GJT3
Main Rupture Area
Subfault with Largest Slip
100 km
[m]
1.0
0.5
0.0
(b)
Observed
Fault model (VR=85.8%)
Relative Pressure [hPa]
20 cm ΔH2O
LT from Foreshock #1 [min]

Figure 2

793

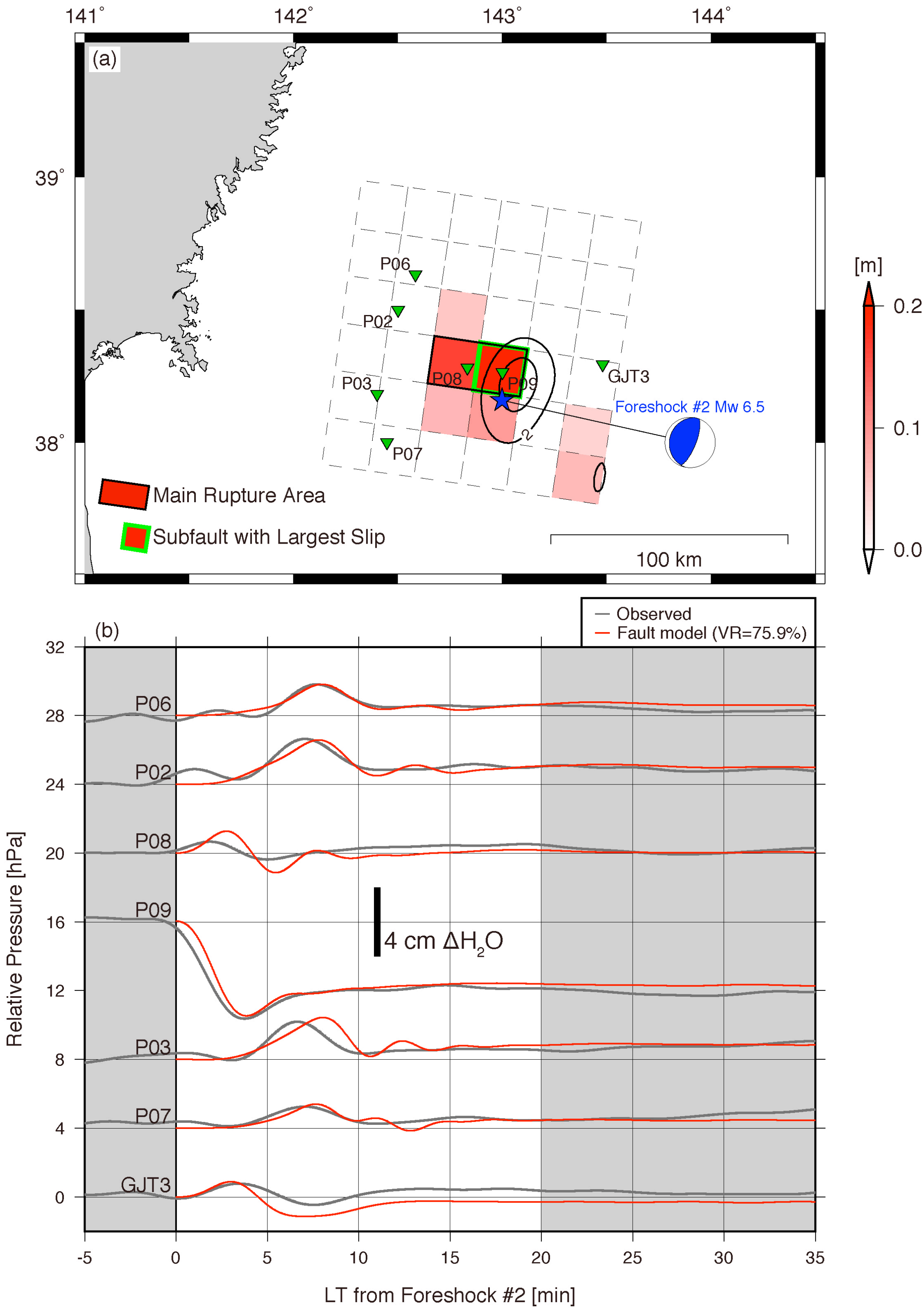

794

795 Figure 3

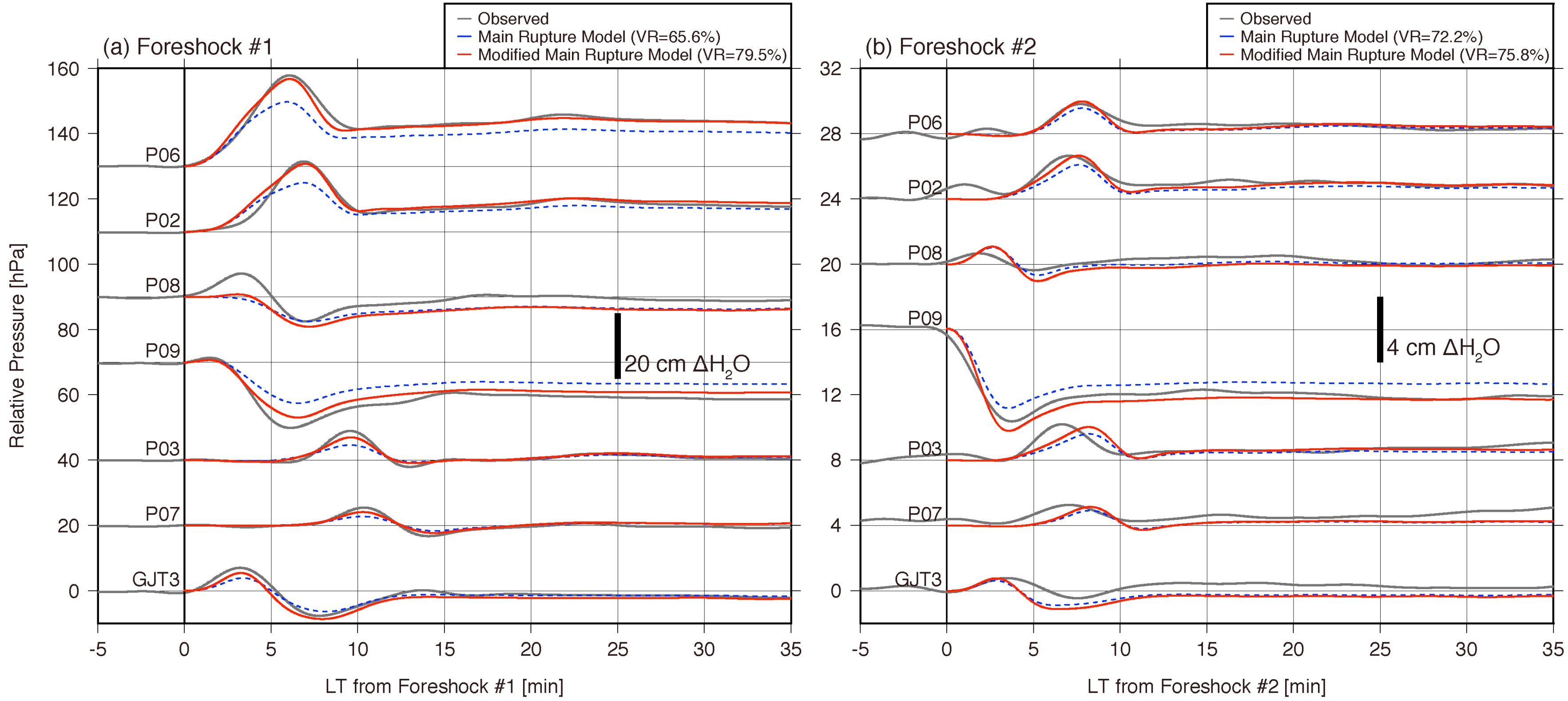
(a) Foreshock #1
Observed
Main Rupture Model (VR=65.6%)
Modified Main Rupture Model (VR=79.5%)
P06
P02
P08
P09
P03
P07
GJT3
20 cm ΔH2O
Relative Pressure [hPa]
LT from Foreshock #1 [min]
(b) Foreshock #2
Observed
Main Rupture Model (VR=72.2%)
Modified Main Rupture Model (VR=75.8%)
P06
P02
P08
P09
P03
P07
GJT3
4 cm ΔH2O
LT from Foreshock #2 [min]

Figure 4

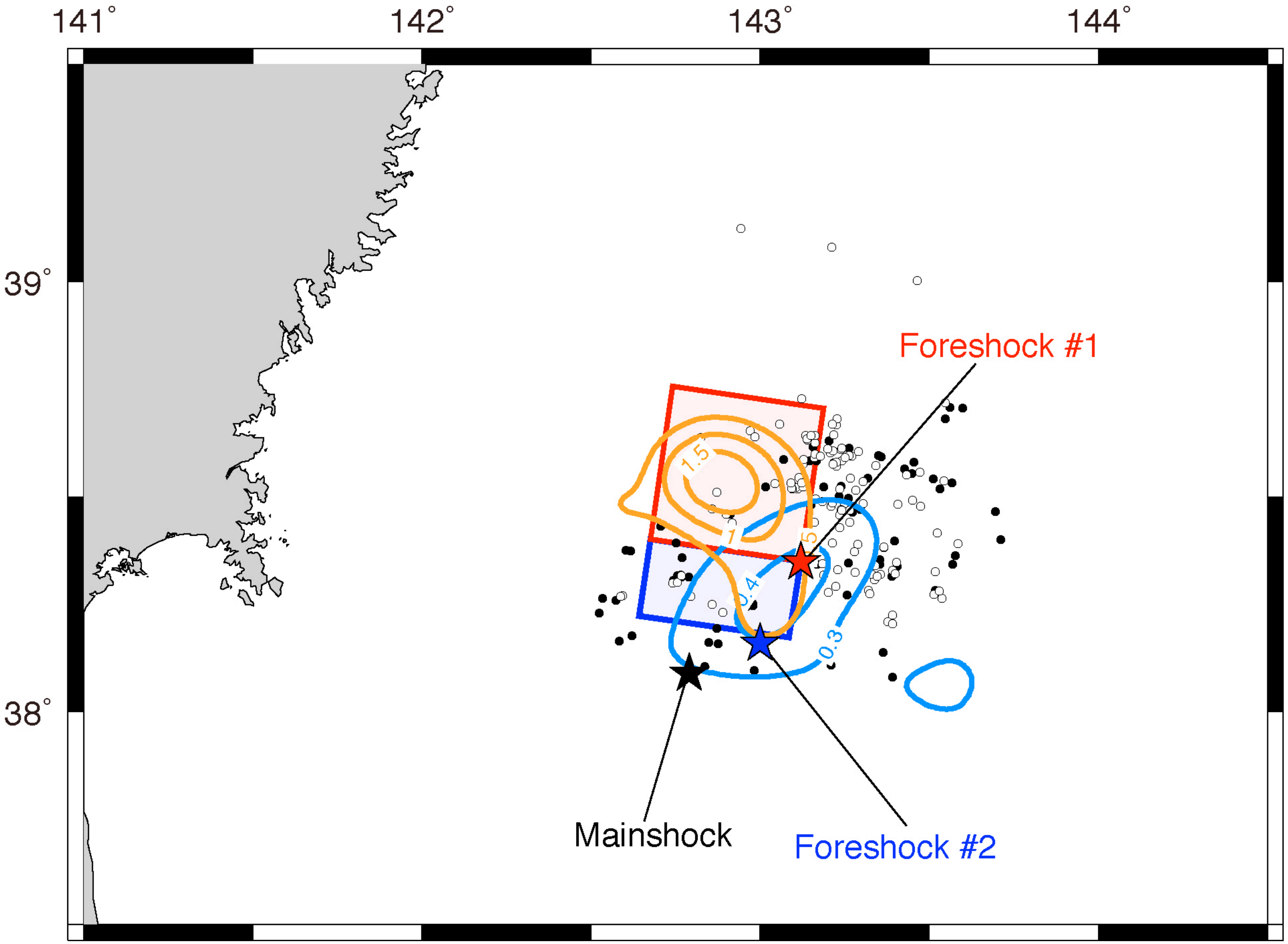
141°
142°
143°
144°
39°
38°
1.5
1
0.4
0.3
Foreshock #1
Mainshock
Foreshock #2

Figure 5

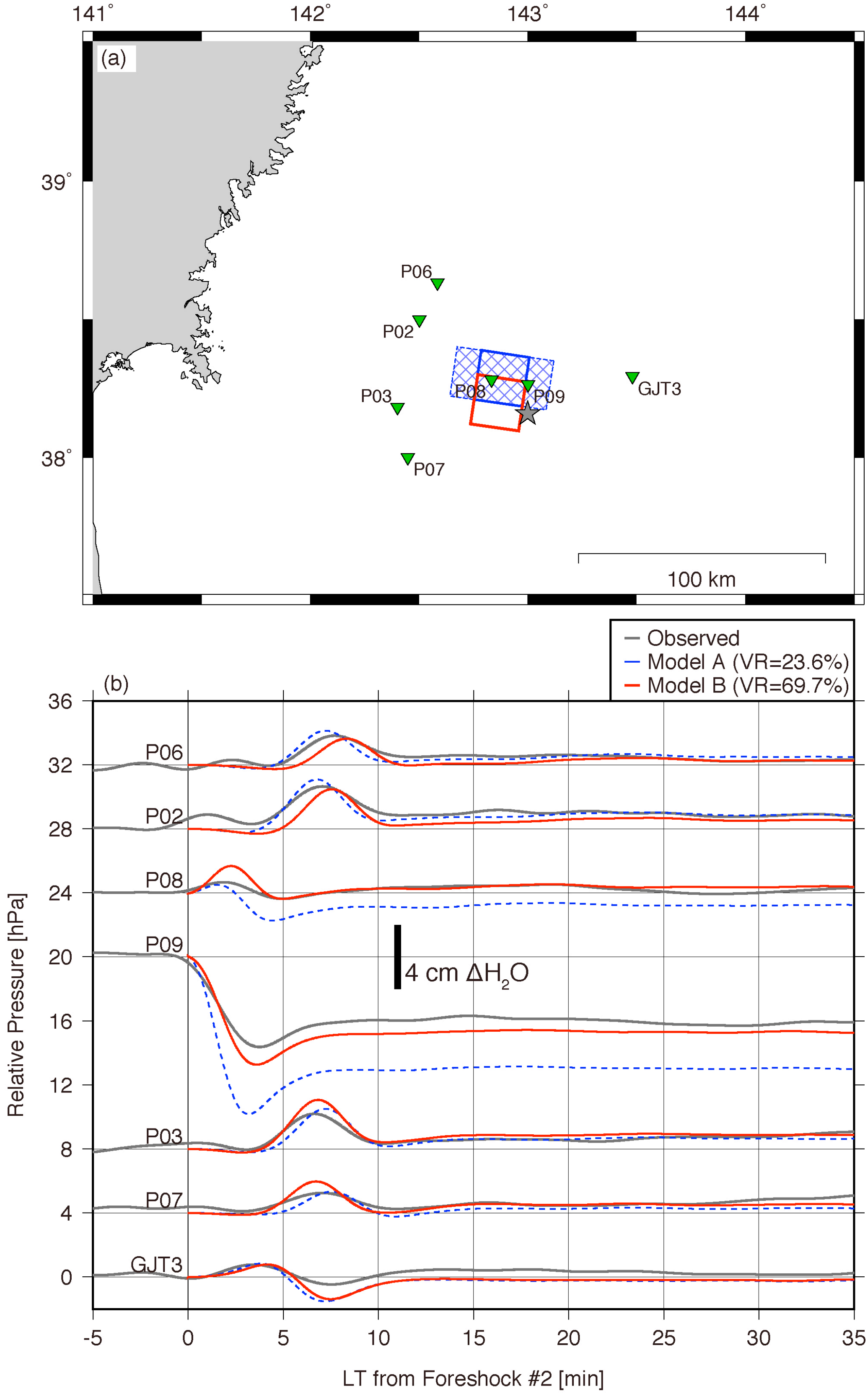
141°
142°
143°
144°
(a)
39°
38°
P06
P02
P03
P08
P09
GJT3
P07
100 km
Observed
Model A (VR=23.6%)
Model B (VR=69.7%)
(b)
36
32
28
24
20
16
12
8
4
0
P06
P02
P08
P09
P03
P07
GJT3
4 cm ΔH_2O
Relative Pressure [hPa]
-5
0
5
10
15
20
25
30
35
LT from Foreshock #2 [min]

Figure 6

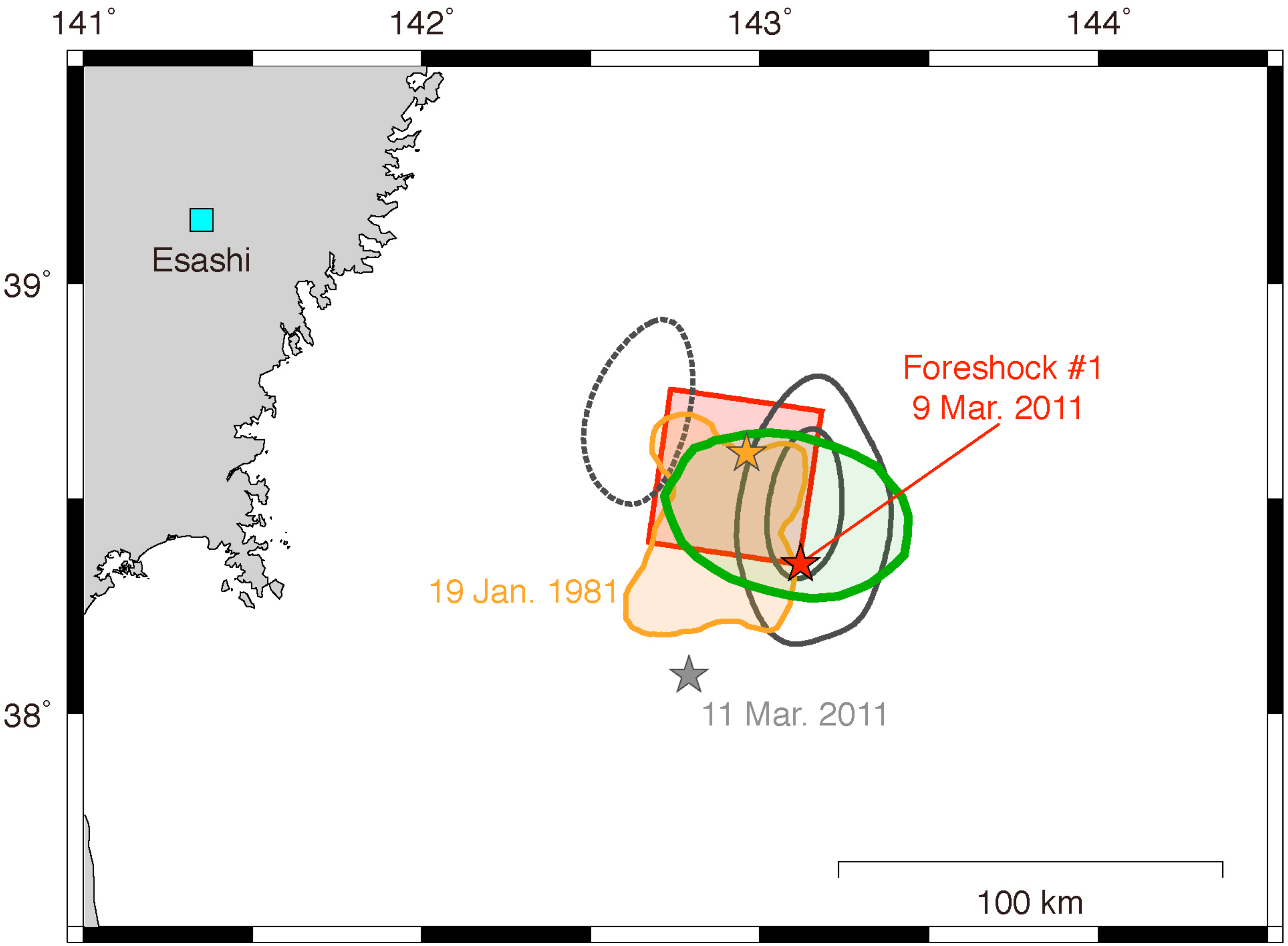
141°
142°
143°
144°
39°
38°
Esashi
Foreshock #1
9 Mar. 2011
19 Jan. 1981
11 Mar. 2011
100 km

Figure 7

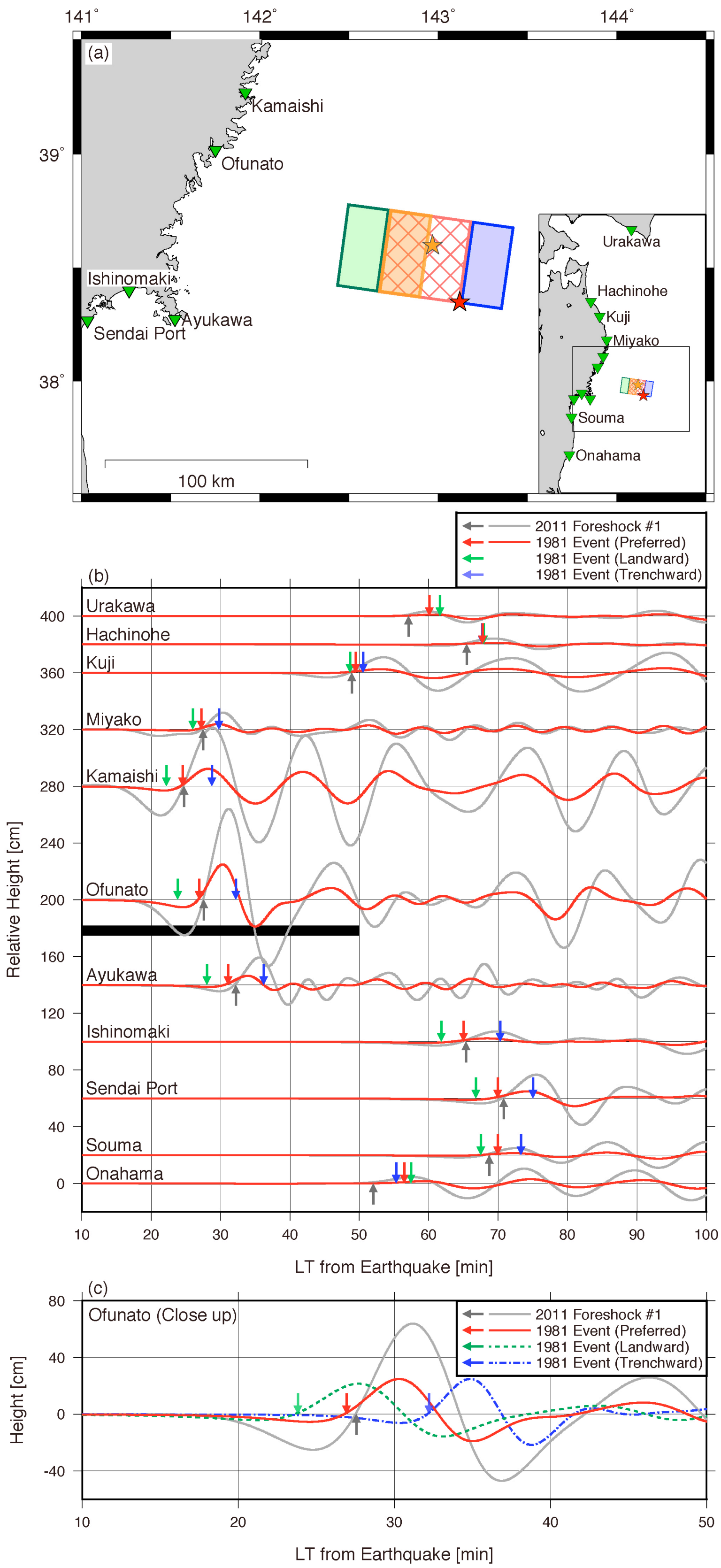

141°
142°
143°
144°
39°
38°
(a)
Kamaishi
Ofunato
Ishinomaki
Ayukawa
Sendai Port
100 km
Urakawa
Hachinohe
Kuji
Miyako
Souma
Onahama
(b)
2011 Foreshock #1
1981 Event (Preferred)
1981 Event (Landward)
1981 Event (Trenchward)
Relative Height [cm]
LT from Earthquake [min]
(c)
Ofunato (Close up)
Height [cm]
LT from Earthquake [min]

Figure 8

Supporting Information

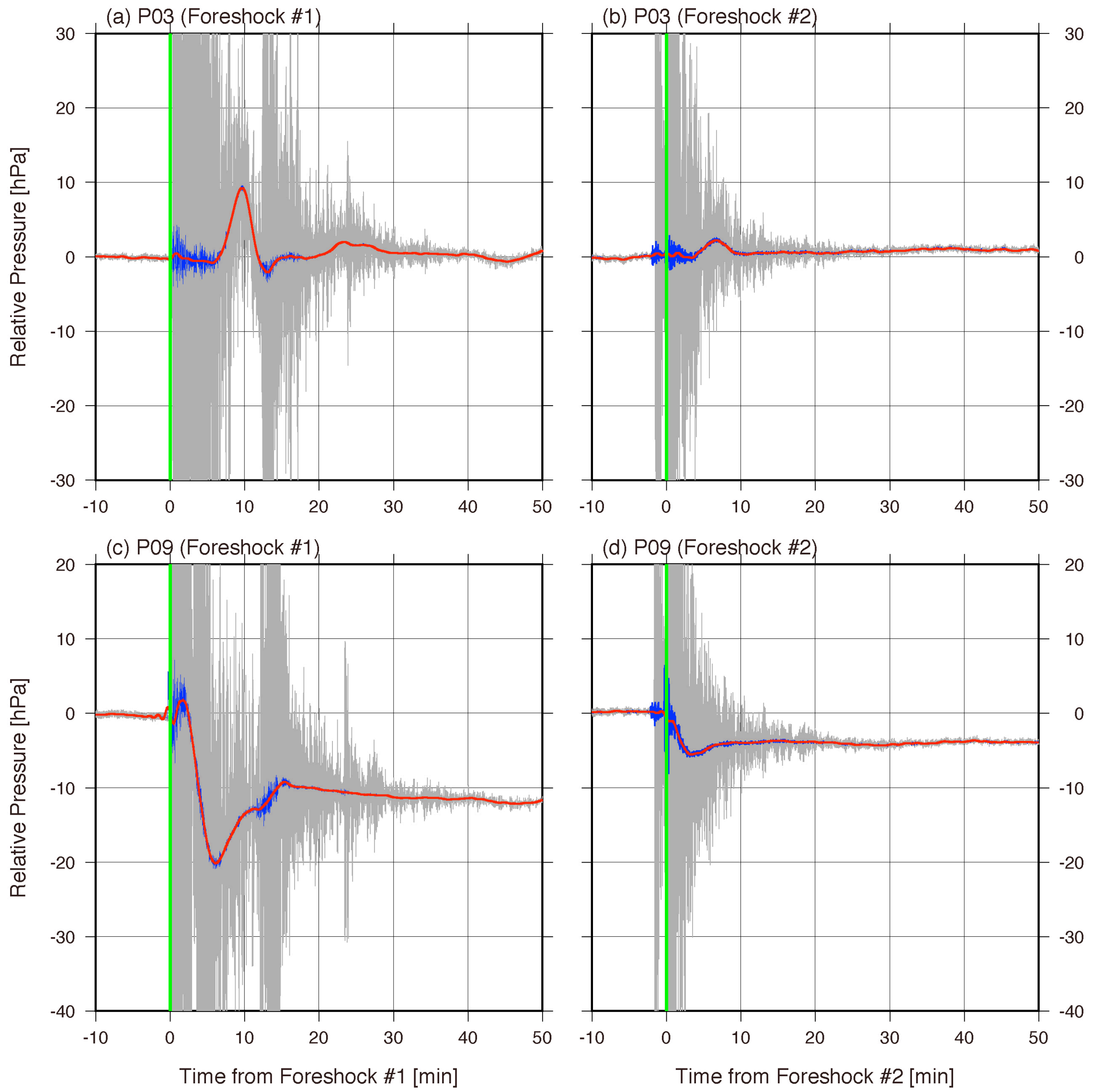

Figure S1. Examples of pressure time series during foreshocks #1 and #2. Time series for (a) foreshock #1 at P03, (b) foreshock #2 at P03, (c) foreshock #1 at P09, and (d) foreshock #2 at P09. Gray, blue, and red traces denote tide-free, 60 s moving averaged and low-pass filtered waveforms, respectively. Green lines denote origin time.

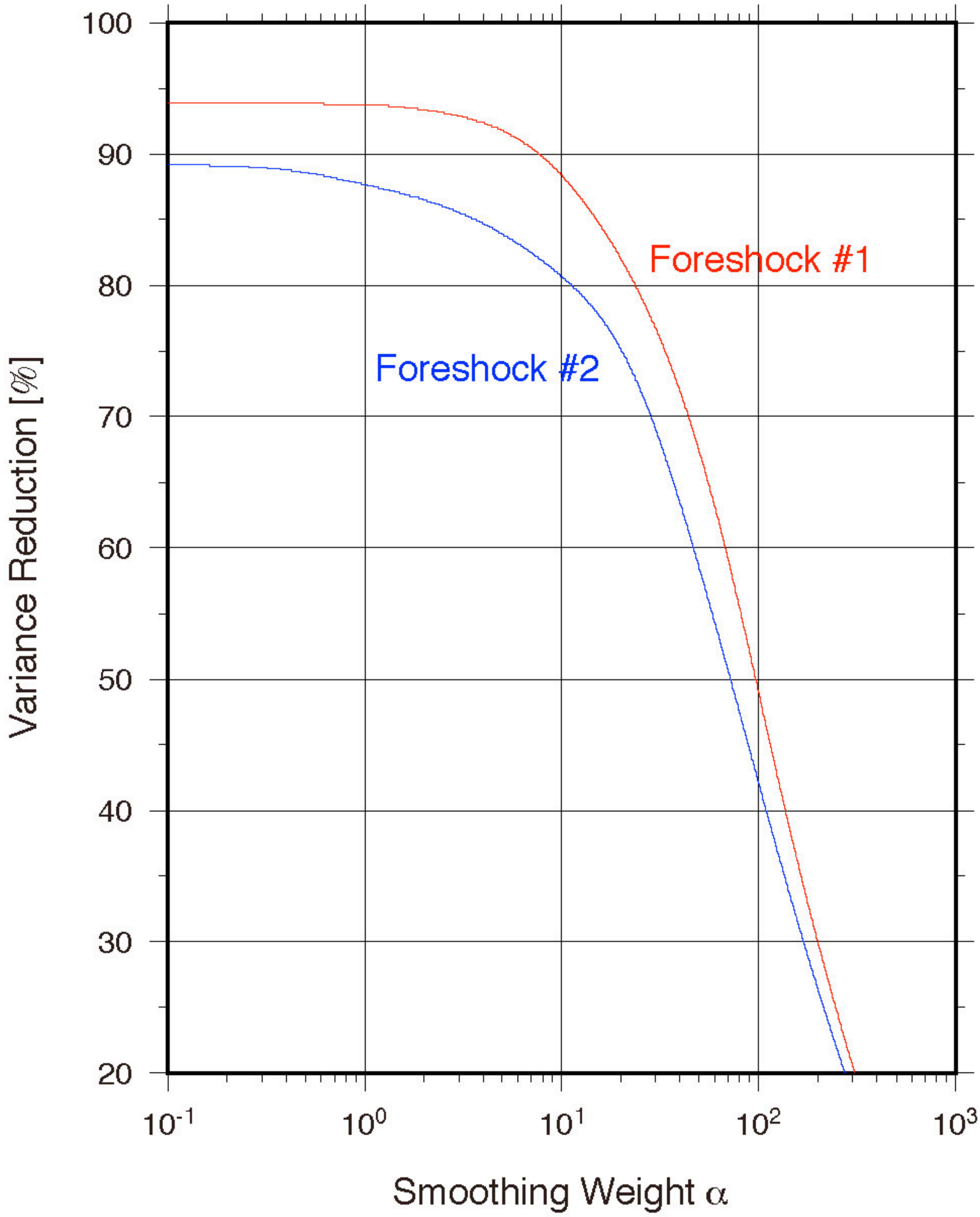

Figure S2. Trade-off curves of waveform inversion for foreshocks #1 (red) and #2 (blue). Weight of smoothing α and variance reduction (VR) are shown in horizontal and vertical axis, respectively.

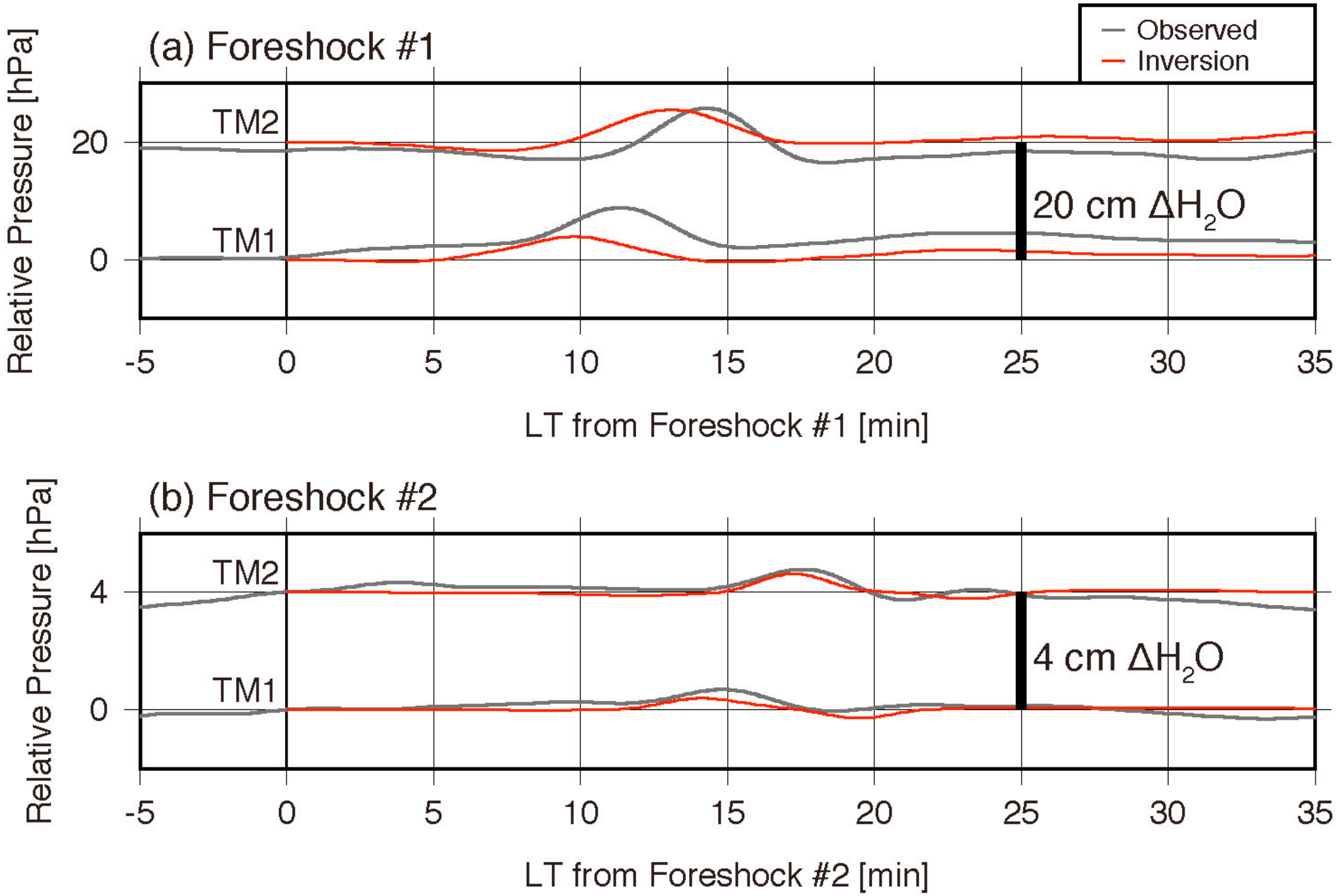

Figure S3. Comparison of observed (gray) and calculated waveforms obtained from inversion result (red) at stations TM1 and TM2 for (a) foreshocks #1 and (b) #2.

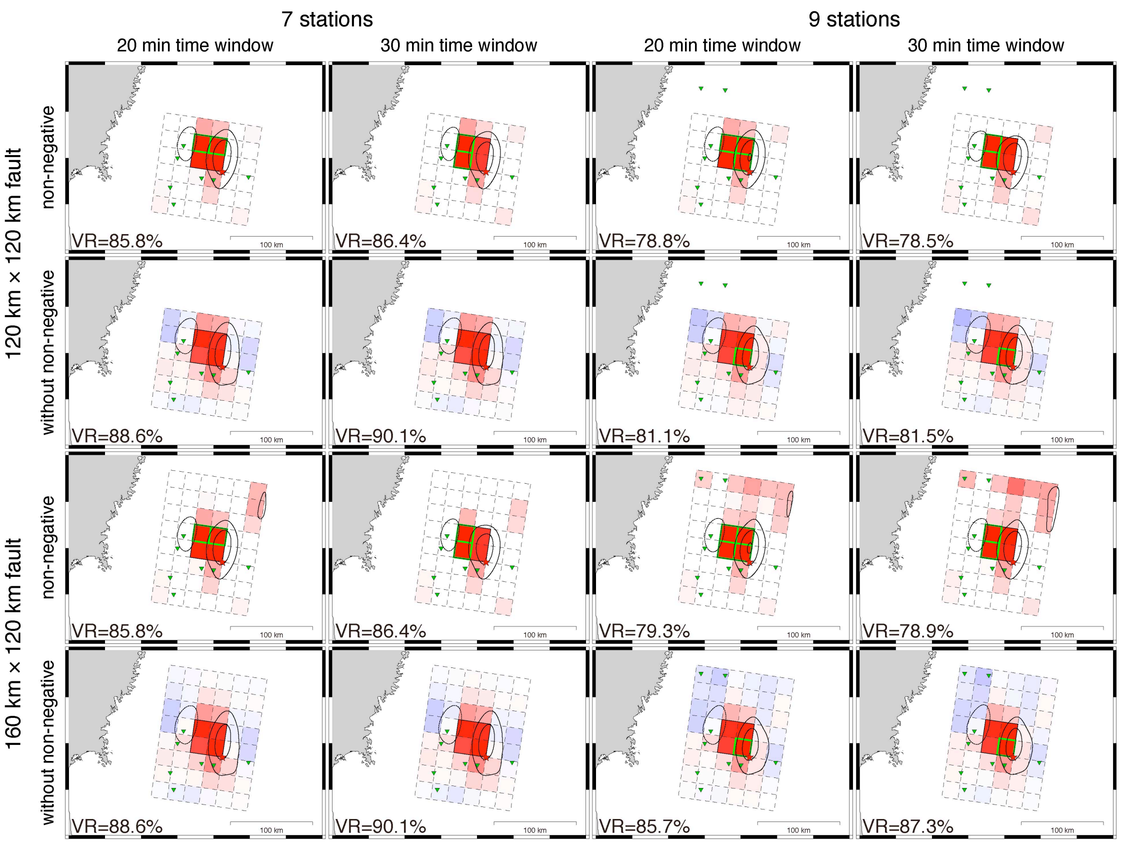

Figure S4. Results of inversions with different conditions for foreshock #1. The conditions are: number of stations (7, without TM1 and TM2, and 9, with TM1 and TM2), along-trench length of mode space (120 km and 160 km), time window length (20 min and 30 min), and inversion constraint (with and without non-negative constraint). Green squares denote subfault with slip larger than 1.0 m.

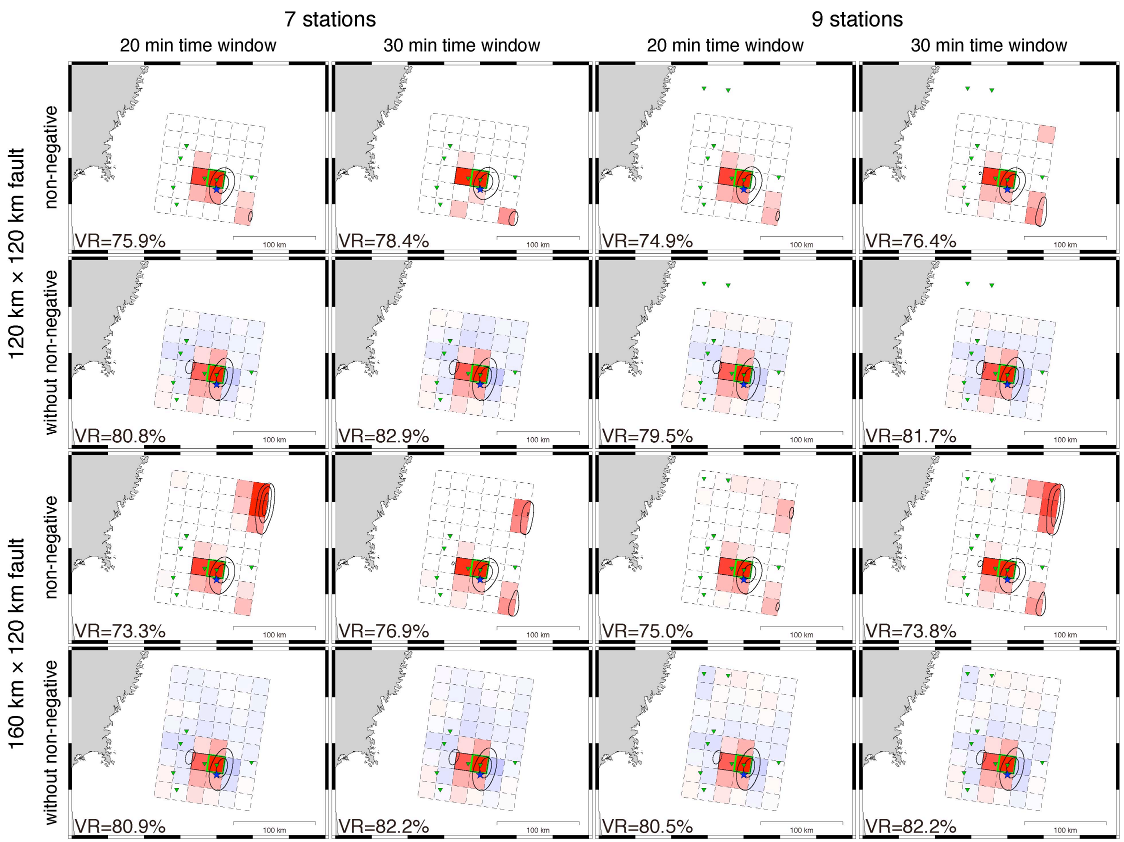

Figure S5. Same as Figure S4, but for foreshock #2. Green squares denote subfault with slip larger than 0.2 m.

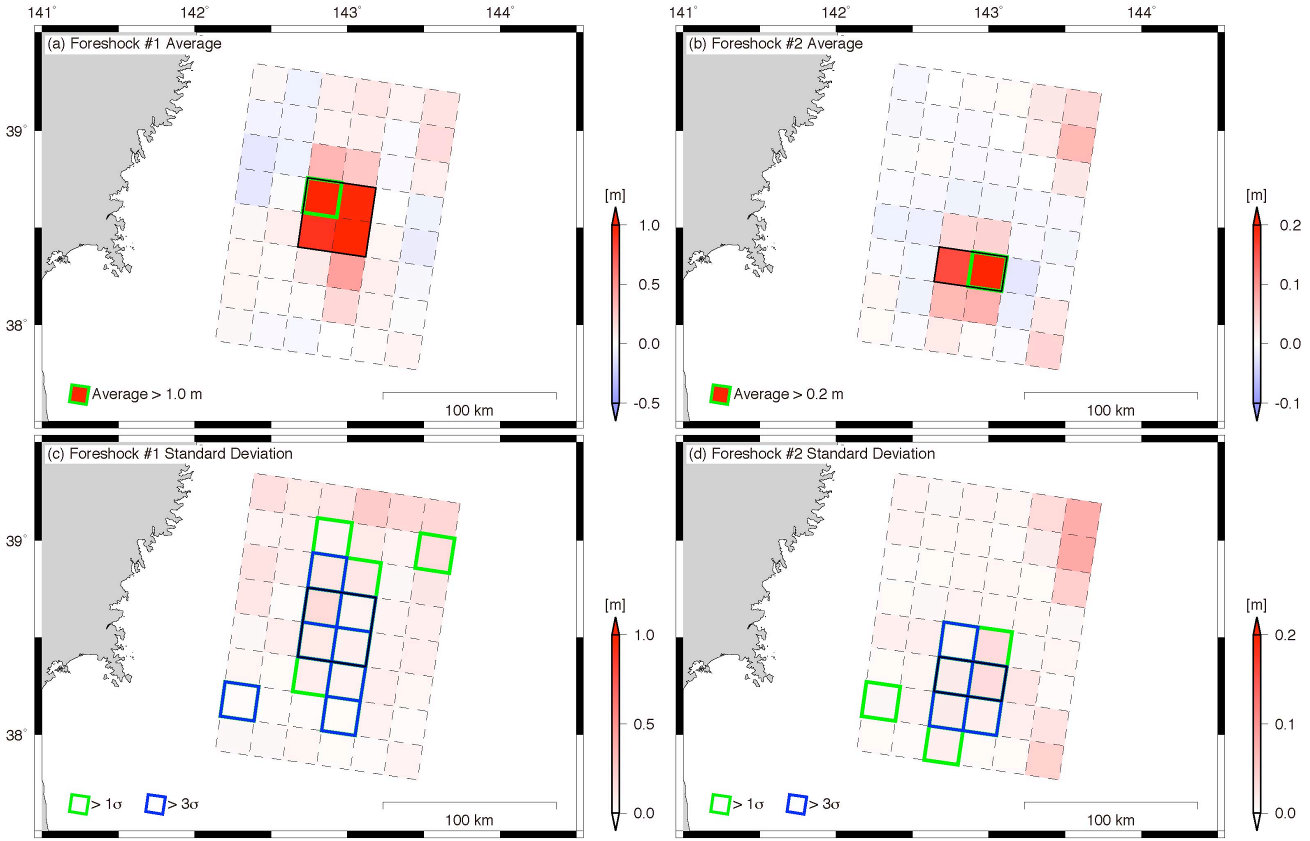

Figure S6. Averaged slip amounts and standard deviations of foreshock #1 (a and c) and foreshock #2 (b and d) calculated from fault models shown in Figures S4 and S5. Averages and standard deviations for 12 subfaults in northern part of model space are obtained from results with a larger model space (160 km length), but those in other subfaults are from all the inversion results.

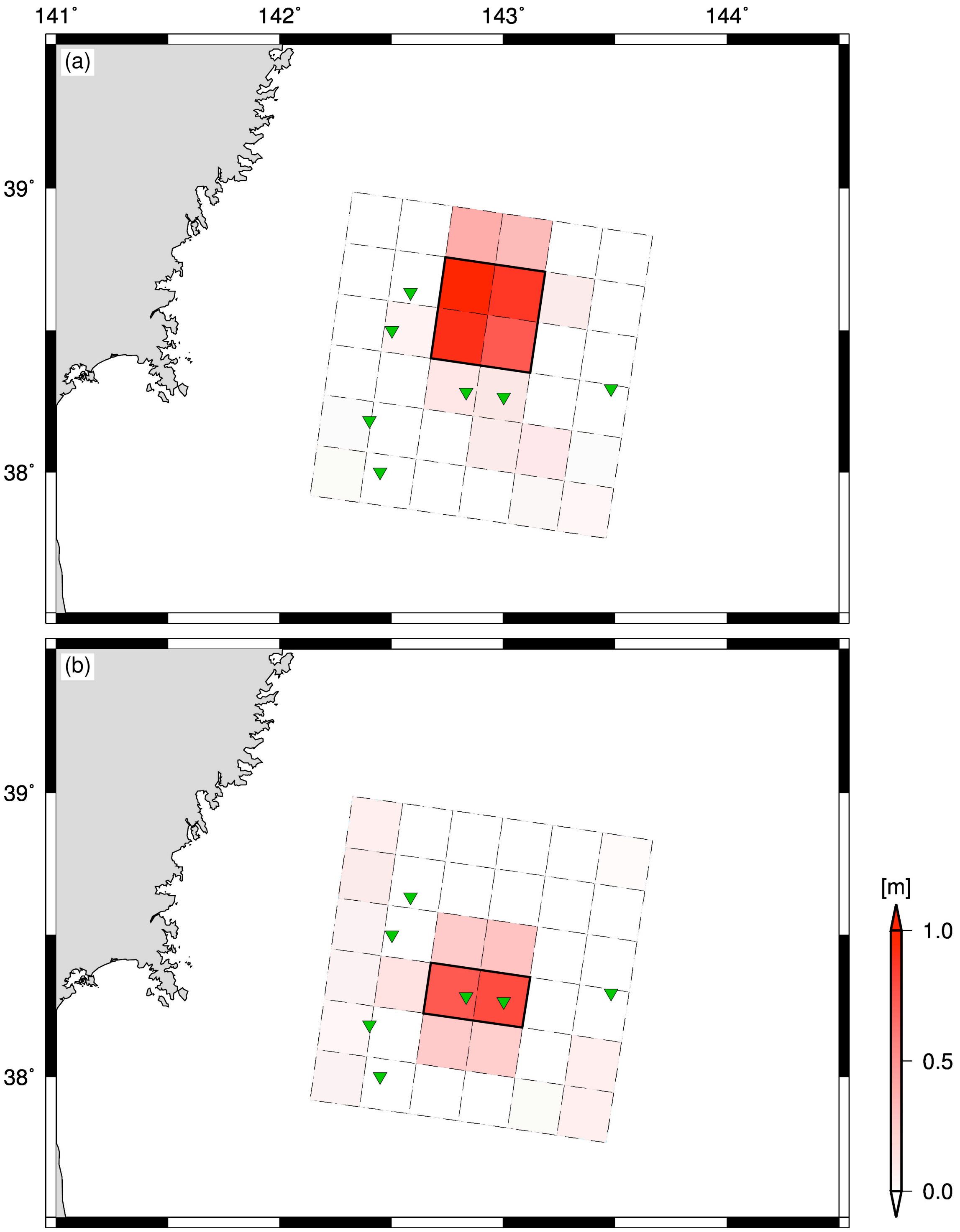

Figure S7. Results of recovery test, giving slips of 1 m for main rupture areas of foreshocks (a) #1 and (b) #2.